Available online at www.sciencedirect.com

SciVerse ScienceDirect

Procedia Engineering 00 (2012) 000–000

Procedia Engineering

www.elsevier.com/locate/procedia

5th BSME International Conference on Thermal Engineering

Investigation of machinability responses during magnetic field assisted turning process of preheated mild steel

Md. Anayet U. Patwari[1], M.N. Mahmood[2], Shafi Noor[3], Md. Ziaul Haque Shovon[4]

Department of Mechanical and Chemical Engineering
Islamic University of Technology
Dhaka, Bangladesh

Abstract

This paper aims to investigate the effects of heat treatment and magnetic field on the machinability responses during turning process of mild steel. Investigation of machinability has been studied by considering the tool life, surface roughness and chip morphology. The effect on the rise in temperature during the turning operation has been studied. In the experimental investigations, heat treated mild steel and normal mild steel has been considered as two work materials. Turning operation tests were conducted using lathe machine with automatic feed at room temperature in dry condition. It has been observed that machinability responses with the combined effect of magnetic field and heat treatment gives significant improvement compared to normal machining process in non heat-treated mild steel. The obtained improvement reflects the feasibility of using this technique as a cost effective turning processes.

Keywords: Mild steel, Annealing, Chip morphology, Machinability responses, Tool wear, Surface roughness, magnetic field

1. Introduction

In machining process using lathe machine, the removal of material from the rotating work piece results in the wear of the tool as the cutting operation proceeds. Tool wear leads to the failure of the tool which affects the cost of manufacturing process. Improving tool life has been the active area of study for quite a long time in order to decrease the cost of machining process. The good machinability factors such as surface roughness, tool life etc. is an important parameters for high precision products. The behavior of chips produced during machining process are also considered as an important factor of machinability. The temperature variation in the cutting contact zone plays a role for the tool life and the surface roughness [1-3]. During turning process the maximum tool wear ($V_{B\,max}$) shows a linear relation with cutting distance after initial rapid wear [4].

Annealing is a process in which a metal is heated to a particular high temperature, held there for a period of time and allowed to cool slowly. Metals are generally annealed at a temperature slightly above the point at which re-crystallization occurs. Annealing is concerned with rendering steel soft, increasing ductility and alleviating internal stresses for better cold work or machining. Annealing also increases toughness and homogeneity of metals [3-5]. Machining of annealed work piece leads to better tool life and reduced surface roughness [3]. In this study, heat treated mild steel and normal mild steel have been taken as two work materials. For the improvement of tool life and surface of the product, the application of magnetic field has proved to have significant effect. The correlation has been established where increasing magnetic field strengths correspond to better tool life [1-2]. The temperature rise during magnetic cutting is higher than that for cutting without magnet. It has been observed that the increase in magnetic field intensity results in further increase in temperature at the contact of tool and the work piece. In this paper, external magnetic field is applied during cutting a heat treated work

Corresponding author. Tel.: 01741180938; fax: 88029291260.
E-mail address: aupatwari@hotmail.com

piece and the results of corresponding tool wear, surface roughness, temperature variations and chip morphology have been studied.

2. Details of experiment

The work piece used in this experiment is mild steel (carbon content of 0.25%) of 40 mm diameter. After the annealing process the hardness of heat treated work piece has reduced significantly. The turning operation has been carried out in precision lathe (Gate INC. Model-L-1/180) under dry cutting condition. The process flow diagram of the experiment is shown in figure 1. The different equipments for preparation, testing and analysis of different parameters like hardness testing machine, optical metallurgical microscope (KRUSS, model MMB 2300) and the heat treatment furnace used in the experiment are shown in figure 2.

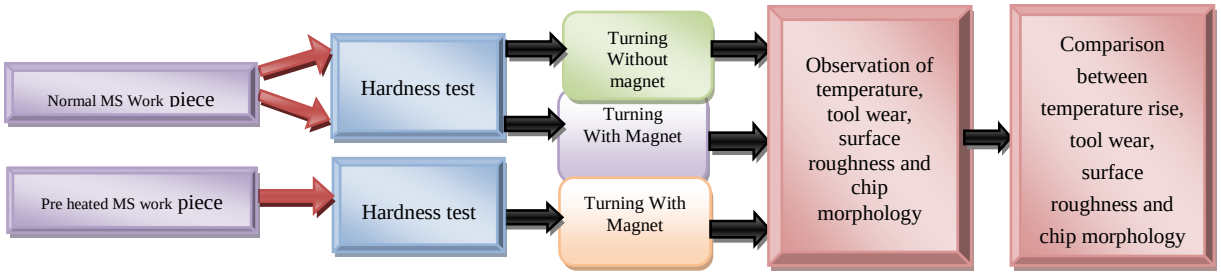

Fig. 1: Process flow diagram and result analysis of the results

Fig. 2: (a) Heat treatment furnace, (b) Rockwell hardness testing machine, (c) Optical metallurgical microscope set up

Three cases have been considered for conducting the experimentation during turning operations. In the experiment, non heat treated work piece without magnet, non heat treated work piece with magnet, heat treated work piece with magnet have been investigated for machinability responses. The experimental setup and the dimension of the tool holder with insert are shown in fig. 3.

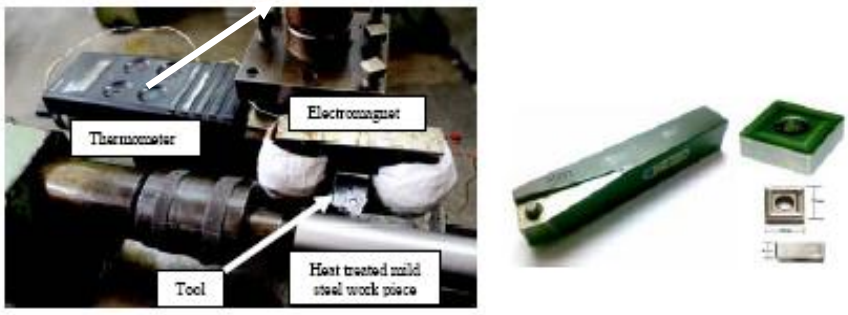

Fig 3: (a) Experimental setup used to study the machining responses during magnetic field assisted turning process, (b) tool holder and insert

The cutting tool insert used in this experiment is coated Tungsten Carbide insert. The cutting condition was selected as feed 0.095 mm/rpm (automatic), depth of cut 0.5 mm and cutting speed 530 rpm. Tool wear was observed using optical microscope at each 200 mm cut of the work piece. To measure the surface roughness, an image processing technique was

used developed by Anayet U. Patwari et al [6-7]. The process flow to determine a linear regression calibration curve for machined surface using digital image processing technique and the process flow to determine the surface roughness of the machined surface is developed by the authors is shown in fig. 4.

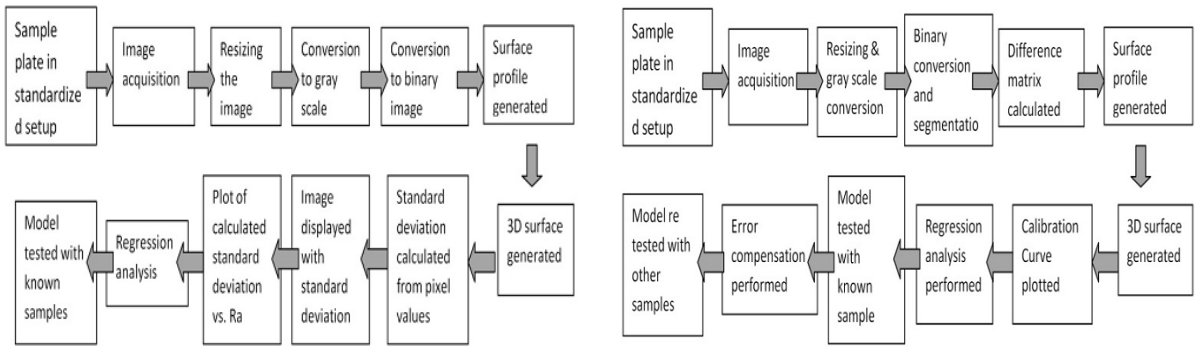

Fig. 4: (a) Flow diagram of the steps to determine a linear regression calibration curve, (b) Flow diagram of the steps to develop 3-D contours and surface roughness.

The mathematical definition of average surface roughness, R_a, was found which is equivalent to half of the mean difference in heights between the asperities and troughs of rough surface. The equation is as follows:

$$R_a = \frac{y_a + y_b + \cdots + y_n}{n} = \frac{1}{n}\sum_{i=1}^{n} y_i = \frac{1}{1}\int_0^1 \left| y \right| dx$$

The rise in temperature after cutting 150 mm of the work piece has been recorded using a thermo couple based digital thermometer, the junction of which was closely attached to the minor cutting edge of the insert, close to the contact point of the tool insert and the work piece.

The chips formed during turning were investigated and it has been found that at some specific cutting conditions chip formation presents extreme cases of secondary and primary chip serration. Firstly, the chip at different cutting conditions were collected, labeled and kept accordingly. Then each chip was mounted using a mixture of resin and hardener. The mixture was stirred for about one minute and left to solidify. The solidified mixture is called mounting. The next step is to grind the mounting surface in order to reveal the chip to the surface. Finally, Nitol is applied to the surface to reveal the grain boundaries of the ferrite and pearlite. Then the mounting is ready to be viewed under the microscope to capture the structure of the chip.

3. Result and Discussion

3.1 Tool life comparison

The pictures of the tool wear taken by the microscope are further processed to measure the tool wear. One sample set of picture of tool wear taken after 600 mm of the work piece is shown in fig.5 for all three conditions of cutting.

Fig. 5: (a) tool wear in cutting normal work piece without magnet, (b) tool wear in cutting normal work piece with magnet, (c) tool wear in cutting heat treated work piece with magnet

After the observation, it is found that the tool life has substantially increased in the case of machining of heat treated work piece with external magnetic field compared to other two cases. The results of tool wear at different length of cut of the work piece are shown in table 1 and the corresponding graph to illustrate the comparative results is given in fig. 6.

Table 1: Tool wear (mm) at different cutting length

Length of cut (mm)	Non heat treated (without magnet)	Non heat treated (with magnet)	Heat treated (with magnet)
200	0	0	0
400	0.057	0.024	0.022
600	0.323	0.135	0.114
800	0.393	0.286	0.196
1000	0.412	0.305	0.254

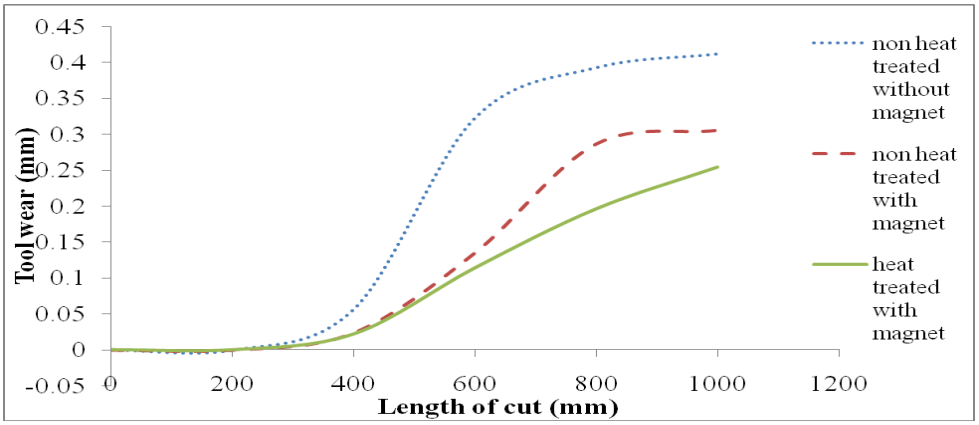

Cutting Conditions	Surface Roughness (μm)	Sample picture taken by the microscope	Contour plot of the surface
Non heat treated work piece machined without any magnet	0.815		
Non heat treated work piece machined with magnet	0.767		
Heat treated work piece machined with magnet	0.655		

ons

al magnetic field during

ed work piece and then

.

Cutting Conditions	Surface Roughness (μm)	Sample picture taken by the microscope	Contour plot of the surface
Non heat treated work piece machined without any magnet	0.815		
Non heat treated work piece machined with magnet	0.767		
Heat treated work piece machined with magnet	0.655		

From the results obtained for surface roughness, it is observed that the surface produced from machining mild steel by applying external magnetic field has less roughness than that produced by machining the work piece without any magnetic field applied. It can be also deduced that the surface improves further when the work piece is pre-heat treated along with the application of magnetic field.

3.3 Temperature variation at different conditions

The rise in temperature after cutting 150 mm of the work piece for 0.5 mm depth of cut with 530 rpm has been investigated for the different cutting conditions. The temperature recorded at different conditions is shown in fig. 7.

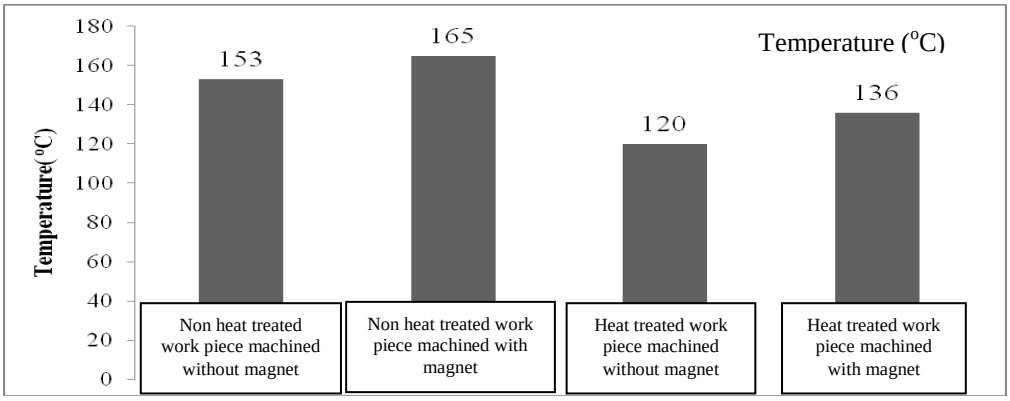

Fig.7: Temperature rise for turning non heat treated and heat treated work piece, with and without magnet

The application of external magnetic field during machining of mild steel results in the rise in temperature at the contact point of the tool and the work piece [1]. This trend is seen in our study also. Since annealing is carried out to soften the material, there is a decreasing tendency of the cutting temperature during machining of annealed work piece than that for machining non heat treated work piece. However, when external magnetic field is applied during machining of annealed work piece, temperature is higher. This study emphasizes on the change in machinability responses in softening mild steel. The increased temperature during electromagnet assisted cutting process contributes to the post hardening of the work piece during machining operation. Thus the annealing method resulting in improved tool life compensates the hardening of the work piece cost.

3.4 Chip morphology:

Continuous chip is produced from turning normal mild steel by applying external magnetic field whereas the chips produced during machining of normal mild steel without any magnetic field are serrated and discontinuous.

Table 3: Results obtained by analyzing the chips from different condition of machining

Curing conditions	Continuity of chips	Microscopic view to show the tooth formation of chips
Non heat treated work piece machined without any magnet		
Non heat treated work piece machined with magnet		
Heat treated work piece machined with magnet		

However when the work piece is heat treated and machined with the application of external magnetic field, the continuity of the chips increases further. The results obtained by carrying out chip morphology are shown in table 3.

The microscopic view of the chips shows that the teeth of serrated chips are larger in size and this size gradually decreases from non magnetic cutting to magnetic cutting which is improved more when a heat treated mild steel is used as the work piece materials.

From the chip morphology study it has been observed that the serrated behavior of chip has been reduced with the combined effect of heat treatment and magnetic field. Surface roughness is often concerned with the adhesion of work material to the tool face. Applying magnetic field reduces this adhesion and produces better surface roughness which is indicated by continuity of chips.

The cross sectional view shows that the teeth formed are smaller in size when magnetic field is applied. This is clear indication of reduction in the amplitude of chatter vibration which results in improved tool life and better surface quality.

4. Conclusion

Significant improvement of machinability factors by using heat treated work piece along with external magnetic field has been achieved in this study. By analyzing all the results the following conclusions can be drawn.

- Combined effect of magnetic field and heat treatment leads to significant improvement in tool life than that of machining of normal work piece. The maximum tool wear $V_{B\,max}$ (~0.3 mm) has been reached after cutting 600 mm in case of non heat treated work piece without magnet, 1000 mm in case of non heat treated work piece with magnet. And in case of cutting with heat treated bar with magnet, the maximum tool wear occurs after cutting the length which is beyond 1000 mm.
- The surface is more polished when magnetic field is used in machining of heat treated work piece than the other two cases. About 20% improvement in surface roughness has been obtained by applying magnetic field in cutting annealed work piece comparing to the surface obtained for normal machining and about 15% improvement in roughness is obtained comparing to magnetic cutting of normal mild steel
- Temperature rises with the application of external magnetic field, but it decreases in case of heat treated work piece.
- Serrated behavior of chips has been reduced in case of magnetic field assisted turning operation of heat treated mild steel.
- This process may be applied to other materials of different strengths for investigating the change in machinability responses due to the application of magnetic field or annealing process before machining operation.

References

[1] M.El Mansori, F. Pierron, D. Paulmier,2003 "*Reduction of tool wear in metal cutting using external electromotive sources*", Surface and Coatings Technology 163 – 164 (2003) 472–477

[2] Anayet U. Patwari, M.N. Mahmood, M.D. Arif, "*Improvement of Machinability of Mild Steel during turning operation by Magnetic Cutting*", International Journal on Advanced Science Engineering Information Technology, Vol. 2 (2012) No. 3

[3] Anayet U. Patwari, N.A. Chowdhury, Md. I. Imam, A. Arefin, M.N. Mahmood,2011 "*Investigation of machinability improvement during operation of heat treated mild steel*", ICME11-ABS000

[4] Chou, Y. K. and Evans, C. J., 1997 "*Tool wear mechanism in continuous cutting of hardened tool steels", Wear 212, 59-65*

[5] Sanjib Kumar Jaypuria, 2008-09, "*Heat treatment of low carbon steel",* National Institute of Technology, Rourkela.

[6] Anayet U. Patwari, Arif M.D., Chowdhury N.A., and Chowdhury Md. S. I., "*3-D contour generation and determination of surface roughness and determination of surface roughness of shaped and horizontally milled plates using digital image processing,"* International Journal of Engineering, Annals of Faculty of Engineering, Hunedoara, Romania.

[7] Arif M.D., Patwari A.U., Chowdhury N.A., *"Surface roughness characterization using digital image processing technique."* Proceedings of the 13th Annual Paper Meet, Mechanical Engineering Department, Institute of Engineers, Bangladesh (2010).

Available online at www.sciencedirect.com

SciVerse ScienceDirect

Procedia Engineering 00 (2012) 000–000

Procedia Engineering

www.elsevier.com/locate/procedia

5th BSME International Conference on Thermal Engineering

Characteristics of CFRP Hydrogen Storage Vessel on Rising Temperature in the Filling Process

Md. Tawhidul Islam Khan[a*] and Masanori Monde[b]

[a]*Department of Advanced Technology Fusion, Saga University, 1 Honjo-machi, Saga 840-8502, Japan*
[b]*Department of Mechanical Engineering,, Saga University, 1 Honjo-machi, Saga 840-8502, Japan*

Abstract

Different types of materials are commonly used for constructing hydrogen pressure vessels. However, carbon fiber reinforced plastic (CFRP) materials are commercially used in hydrogen vessels now a day. Commercially used aluminium liner vessel is easy to construct and posses high thermal conductivity compared to other commercially available vessels. However, compared to CFRP liner vessel, it has low strength capacity and safety factors. Therefore, now a day, CFRP liner vessels are becoming more popular in modern hydrogen vehicle systems. Moreover, CFRP vessel has light weight advantage. CFRP, although, has many desirable properties in reducing the weight and in increasing the strength, it is also necessary to keep the material temperature below 85°C for maintaining stringent safety requirements. Because while filling process occurs, the temperature can be exceeded due to the compression works of the gas flow. Therefore, it is very important to optimize the hydrogen filling system for avoiding temperature rise to cross the critical limit of damaging CFRP wall vessel.

Computer simulation has been conducted to characterize the CFRP storage vessel in hydrogen filling to optimize the technique. Three hydrogen vessels with different volumes and with different filling pressure have been used to characterize the temperature rise of the wall materials in filling system. The wall materials have been considered as aluminum liner material and CFRP composite materials. Supply tanks have been played important roles in supplying hydrogen in different storage tanks with different supply pressures. Gas temperatures have been measured inside representative vessels in the supply reservoirs and at the inlet to the test tank during filling. In simulation, the geometry has been simplified to a cylinder for illustration purposes. The rise in temperature of the hydrogen and the tank wall during the filling of hydrogen into the actual tank with CFRP liner has been simulated with different filling conditions at Saga University and the results have been compared with JARI (Japan Automobile Research Institute) experimental data as well.

Keywords: CFRP hydrogen vessel; hydrogen filling system; thermal properties; vessel safety.

Nomenclature

A	vessel internal surface area (m^2)
l	total thickness of the wall (m)
P	pressure (MPa)
Q	heat loss into wall, (kJ)
T	temperature (°C or K)
t	time (sec)
x	argument in the x-direction

* Corresponding author. Tel.: +81-952-28-8628; fax: +81-952-28-8587.
E-mail address: khan@me.saga-u.ac.jp

Greek symbols	
λ	thermal conductivity (W/mk)
α_h	heat transfer coefficient at inner surface (W/m^{2}K)
α_e	heat transfer coefficient at outer surface (W/m^{2}K)
Subscripts	
g	gas
s	solid
wi	wall inside
wo	wall outside

1. Introduction

The introduction of fuel cell vehicles (FCV) to public within few years faces lot of challenges. Designing of hydrogen storage tanks as well as fueling systems are the most remarkable items in these challenges. Hydrogen has a very high energy content by weight (about three times more than gasoline), but it has a very low energy content by volume (about four times less than gasoline). This makes hydrogen a challenge to store, particularly within the size and weight constraints of a vehicle. Moreover, Developing safe, reliable, compact, and cost-effective hydrogen storage technologies is one of the most technically challenging barriers to the widespread use of hydrogen as a form of energy. To be competitive with conventional vehicles, hydrogen-powered cars must be able to travel more than 300 miles between fills. This is another challenging goal because hydrogen has physical characteristics that make it difficult to store in large quantities without taking up a significant amount of space.

Lot of efforts have been taken for designing the storage tanks for FCV system. Until now, a CFRP composite material for constructing the pressure vessel for storing hydrogen is widely familiar. CFRP is very strong and light weight. However, it is necessary to keep the material temperature below 85°C under a regulation. Since it is possible to exceed this temperature as a result of the compression work in the filling process, it is desirable to be able to predict the temperature rise prior to commencing refuelling. However, controlling the temperature is one of the key technologies, because the temperature of the hydrogen during filling up to 70 MPa (which is designed to be needed) rises the temperature beyond the temperature limit of CFRP tank. Particularly, in the fast filling system up to 70 MPa in hot summer days, the temperature of the tank can go beyond the temperature limit easily (Khan et al., 2009). Therefore, the reserved hydrogen should be kept cool or the filling system of hydrogen should take enough precautionary measures so that the hydrogen temperature does not exceed 85°C.

Therefore, simulations have been conducted for optimizing the filling system of hydrogen fuel to the storage tank. Different filling conditions, particularly for different heat transfer coefficients of hydrogen gas for grasping the temperature behavior in the hydrogen storage tank have been adopted in the simulation. Experimental data of JARI has been utilized for comparing the simulation results as well.

2. Configuration Analysis

2.1. Storage vessel

Three types of hydrogen storage vessels with different volumes have been considered. However, only one test vessel has been analyzed for optimizing the filling prediction. The wall materials of each test vessel were considered CFRP composite materials along with liner material as aluminium (Al). The schematic configuration of a CFRP hydrogen storage vessel is shown in Fig. 1(a) and its diagonal cross-sectional view is shown in Fig. 1(b). As shown in the figure, one control valve

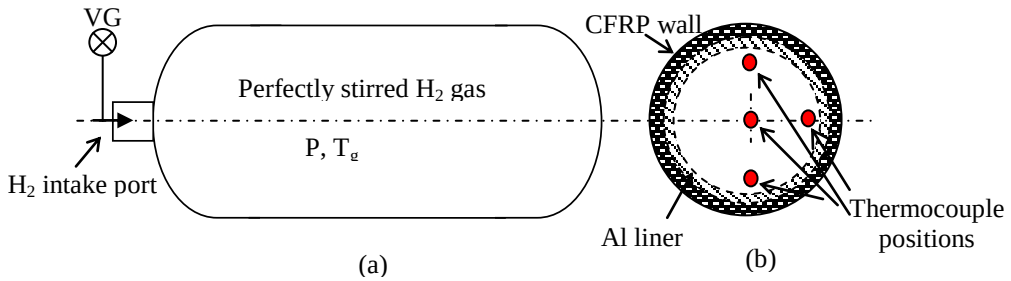

Fig. 1. (a) Schematic of H_2 gas reservoir; (b) cross-section of the reservoir and the thermocouple positions.

Table 1: Vessel specifications and wall properties

Specifications of hydrogen vessel			
Length (m)	O. Diameter (m)	Wall thickness (m)	
0.832	0.4	0.017	
Liner Parameters			
Thickness (m)	Th. Conductivity (W/mk)	Sp. Heat (J/kgK)	Density (kg/m^3)
0.003	180.0	896.0	2700.0
CFRP parameters			
Thickness (m)	Th. Conductivity (W/mk)	Sp. Heat (J/kgK)	Density (kg/m^3)
0.015	1.14	1075.0	1374.0

(VG) is installed at the inlet port of the storage tank for measuring the inlet temperature and inlet pressure of hydrogen gas. The gas pressure and gas temperature inside the vessel are mentioned as P and T_g respectively. The locations of temperature sensors (thermocouple) for getting the sample data in JARI experiments are shown in the figure as well. The wall materials of the tank which influence largely in heat transfer procedure are standardized in the simulation by taking their standard thermal properties as shown in Table 1. Details of the experimental apparatus and procedures of JARI 's experiment is not included here. Only the parameters related to the simulation are mentioned in this paper.

2.2. Filling system

In simulation process, one hydrogen storage vessel (D34L: Japan Automobile Research Institute (JARI) tank) has been used to verify the optimization technique with different filling conditions. The thermal characteristics due to filling system have been analyzed for the examined vessel. The supply system is divided into three storage system having vessels initially at 44 MPa and 87.5 MPa. This configuration is suitable for charging test vessels to 70 MPa. For 35 MPa runs only storage 1 has been required. Similarly for rising higher pressure than 35 MPa, other storages are used. Major objectives of the simulation were ascertained for optimizing the hydrogen filling system to the vessel based on several conditions; such as (i) space average gas temperature at all points in time during and after charging, (ii) final mass of hydrogen in the vessel, (iii) temperature of the wall inside surface, liner/CFRP interface and outside wall surface, (iv) temperature distribution in the wall at a desired point in time. The inlet of the flow system to the vessel plays an important role for the valve system and supply line (due to the negative Joule-Thomson effects). Furthermore, the inertial and compression effects of hydrogen flow in the supply line influence in rising gas temperature in the tank as well. The radiation loss in the flow line does not considered in the calculation, because it is considered as perfectly insulated.

2.3. Thermodynamic modelling

In modelling the system, the geometry of the vessel is simplified to a cylinder for illustration purposes. Although, the program does not care about the shape of the vessel, only the volume and the inside surface area are considered important for simulating temperature rise in filling system. For simplicity, it is assumed that the hydrogen gas is well stirred within the vessel so that the values of gas density and specific internal energy throughout the vessel inside remain constant. Moreover, it is also assumed that the hydrogen supply volume is much larger than the vessel, so that the supply properties do not change during charging. As it is mentioned earlier that the flow work is done as hydrogen is compressed inside the vessel in filling, it causes temperature rise and heat is transferred to the wall by convection. Therefore, finally, the wall temperature rises and finally heat is lost to the surroundings by convection process. In order to evaluate this phenomena, heat transfer rate is calculated from following simple formula (Monde et al., 2007).

$$\frac{dQ}{dt} = -A\lambda \left.\frac{\partial T_s}{\partial t}\right|_{x=0} \qquad (1)$$

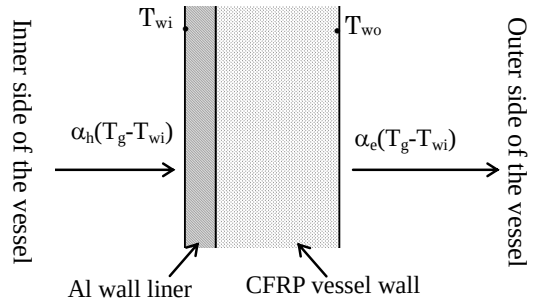

Fig. 2 Schematic figure of vessel wall and its thermodynamic modelling

where, λ indicates the thermal conductivity, A indicates the internal surface area of the vessel. The parametric notation, x indicates the argument in the x-direction across the thickness of the wall. As the combined wall of the vessel is assumed as one-dimensional solid, its temperature is indicated by T_s . Therefore, to simplify the above equation and to determine the wall temperature, the unsteady heat conduction equation can be applied by the following boundary conditions (Woodfield et al., 2008).

$$-\lambda_s \left.\frac{\partial T_s}{\partial x}\right|_{x=0} = \alpha_h \left(T_g - T_s|_{x=0}\right) \tag{2}$$

$$-\lambda_s \left.\frac{\partial T_s}{\partial x}\right|_{x=l} = \alpha_e \left(T_s|_{x=l} - T_{wo}\right) \tag{3}$$

In the above equation, the suffices, s indicates the parameters of solids (combined vessel wall). Moreover, as the gas is assumed as well stirred, it is considered here as, $T_{wi} \equiv T_s|_{x=0}$, where T_{wi} indicates the wall inside temperature. The wall outside temperature is indicated by T_{wo}. Moreover, α_h, α_e indicate the heat transfer coefficients at inner and outer surfaces respectively and l indicates the total thickness of the wall. This thermodynamic model is shown schematically in Fig. 2. One important consideration in the present modelling is that there is zero contact resistance between the surfaces of aluminium liner and CFRP vessel wall.

3. Results of Thermal Characterization of CFRP Hydrogen Vessel

3.1 Performance analysis in temperature estimation

The temperature rise of hydrogen gas inside the vessel as well as the vessel wall due to the filling system as described above is shown in Fig. 3. The estimation of this temperature rise of the storage vessel is predicted by using the software developed by Monde et al. 2007. The calculation is performed based on the energy balance as described above. The measured pressure in the tank during continuous filling to 35 MPa is also shown in the figure. After the vessel has been charged the determination of pressure is necessary and in the present model, it is done based on the Lee-Kester formulation. Furthermore, it is considered that the pressure changes linearly until it reaches to the final pressure (35 MPa). After getting its final pressure (when closing the inlet valve), the pressure remains constant. When the gas attains its final pressure, the temperature is also raised to its ultimate position. In the figure, it is found that gas temperature is raised to around 80 °C from its initial temperature at around 20 °C. As the gas temperature increases, the heat transfer occurs from gas to vessel wall and wall to the atmosphere as explained in the above model. The estimated result is also compared with the JARI experimental data which shows a clear agreement with the estimation process by the developed software. It is also mentioned that the temperature rise of the reservoir varies remarkably based on the filling time. For the quick filling, temperature rises largely compared with the slow filling (Khan et al. 2009). Moreover, there are a lot of parameters that influences the rise of temperature of the vessel as mentioned in the following sub-sections.

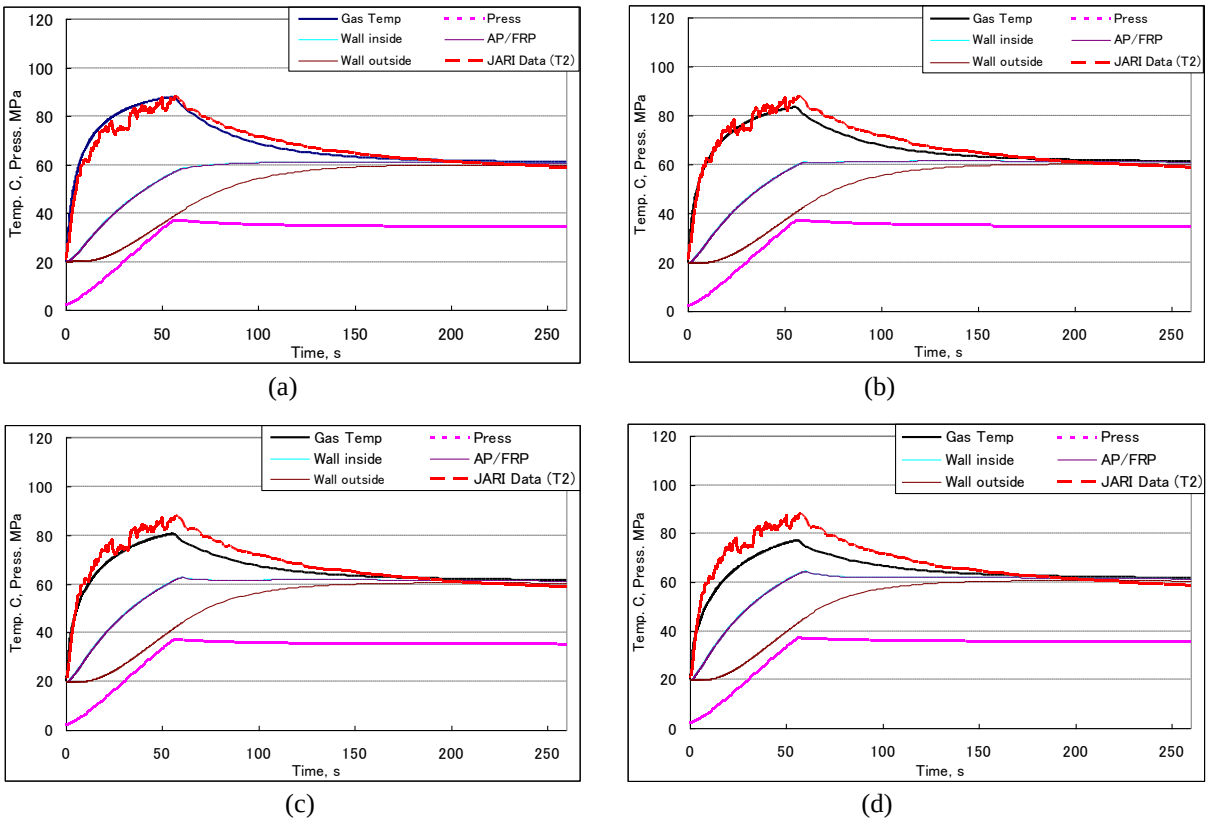

Fig. 3 Temperature profile of test vessel for 60 seconds fill. JARI Data is for comparison of estimated data. Heat transfer coefficients in W/m^{2}K (gas to liner-liner to CFRP-CFRP to outside) are (a) 300-250-4.5, (b) 400-250-4.5, (c) 500-250-4.5, (d) 700-250-4.5.

3.2 Effect of heat transfer coefficient on temperature rise

The influence of temperature rise of the hydrogen gas inside the vessel on various heat transfer coefficient is also verified with the developed software. The results are shown in Figs. 3(a) – 3(d). It is found in the analysis that the calculation result of hydrogen gas at the center of the vessel largely differs for different heat transfer coefficient keeping other test conditions (Table 1) same. Furthermore, as mentioned earlier that the CFRP vessel is the most suitable consideration to the automobile companies, in the present simulation, only the value of heat transfer coefficient of gas to wall (liner) is investigated and therefore, the value of heat transfer coefficients for the vessel wall (liner and CFRP) have been kept constant. In results (Fig 3) it is found that the temperature rising of the hydrogen gas inside the vessel can be controlled effectively (around 10 – 15 °C reduction as shown in the present simulation results) reduced by controlling the heat transfer coefficient of gas to wall. Thus, it would be a considerable thinking for the reduction of the compression works of the filling process for adopting the advantages of the present results.

4. Discussion

In the present paper the thermal characteristics of hydrogen vessel is presented only for one type of storage vessel. However, the varied thermal properties for various storage vessels affect the characteristics of temperature rise as well. For example, the nozzle effect plays an important role in the initial temperature of hydrogen gas as mentioned earlier. Moreover, the filling time is another factor for controlling the temperature rise inside the vessel (Khan et al., 2009). The heat transfer coefficient for the outside of the tank (α_e) is set to 4.5 W/m^{2}K for all calculations, although its value has almost no effect on the present heat transfer analysis. Furthermore, it should be noted that the available temperature does not correspond to the actual gas temperature at the tank inlet, as the temperature sensor by which the temperature has been measured in the

experiment, has been located far from the lank inlet. Unfortunately, no information is available about the data that how far the sensor has been placed.

It is considered in the present calculation that the hydrogen vessel is well stirred. However, Woodfield et al. 2007 mentioned that during the filling of hydrogen the heat transfer coefficient varies in an wide range depending on filling mass flow rate and thus that value is strongly influenced by the location and this effect increases as the location becomes farther from the inlet. On the other hand, when the hydrogen is discharged the heat transfer coefficient is almost independent of the location and its value continuously decreases as the mass flow rate decreases. Therefore, although, the mass flow rate is almost identical in filling and discharging, the heat transfer coefficient behaves with different trends. Thus it is found in the present calculations temperature rise is greatly influenced by this thermal properties. Another important factor in this regard is that heat transfer coefficients are quite different depending on not only the position but also on the time after the filling. In the present model it is assumed that αh is constant for the total filling time. However, practically it varies with the mass flow rate and the changes of gas pressure inside the vessel. Therefore, carefulness is necessary, although, a suitable constant value of heat transfer coefficient is considered in the present model for calculating the temperature rise in gas as well as in vessel wall.

5. Conclusions

Thermal characteristics of hydrogen gas of the storage vessel as well as of the vessel wall have been analyzed successfully by the developed software (Monde et al. 2007). The parameters adopted in the present simulation are considered based on different experimental and simulation data conducted at Saga University as well as at JARI. From the analysis it is clearly understood that for the safety of CFRP hydrogen storage vessel, controlling of rising temperature in the filling process is an important factor and thus, the adjustment of the heat transfer coefficient of filling gas can play an influential role for that purpose.

Acknowledgements

Authors would like to express appreciation to Japan Automobile Research Institute (JARI) for the experimental support to this research.

References

[1] Khan Md. T. I, Monde M, Setoguchi T. Hydrogen gas filling into an actual tank at high pressure and optimization of its thermal characteristics, J. Thermal Science 2009; 18: 235-240.
[2] Monde, M, Mitsutake Y, Woodfield P. L, Maruyama S. Characteristics of heat transfer and temperature rise of hydrogen during Rapid Hydrogen Filling at High Pressure. J. Heat Transfer – Asia Research 2007; 36: 13-27.
[3] Woodfield P. L, Monde M, Takano T. Heat transfer characteristics for practical hydrogen pressure vessels being filled at high pressure. J. Therm Sci Tech 2008; 3(2):241-53.
[4] Woodfield P. L, Monde M, Mitsutake Y. Measurement of average heat transfer coefficients in high-pressure vessel during charging with hydrogen, nitrogen or argon gas. J Therm Science Eng 2007; 2(2):180-90

Available online at www.sciencedirect.com

SciVerse ScienceDirect

Procedia Engineering 00 (2012) 000–000

Procedia Engineering

www.elsevier.com/locate/procedia

5th BSME International Conference on Thermal Engineering

Frictional Heating in Hip Implants – A Review

M. S. Uddin* and P. Majewski

School of Advanced Manufacturing and Mechanical Engineering
University of South Australia, Adelaide, SA 5095, Australia

*Email: mohammad.uddin@unisa.edu.au

Abstract

Frictional heating at the head-cup interface causes temperature rise in the bearing components and the synovial fluid of hip implants. High temperature, not only, causes creep, wear, oxidation of the components, e.g. UHMWPE cup, but also increases the risk of damage to surrounding soft and hard tissue, resulting in the aseptic loosening failure. The present paper reviews studies on frictional heating in hip implants available in literature. The aim, particularly, is to explore mechanism of heat generation due to friction, quantification of temperature rise, and important parameters impacting heat generation. Concerns with the issue are addressed and the importance of the need for potential remedies to minimize the effects is highlighted. The discussion would provide guidelines, enabling biomedical engineers to help design, develop, and implement implants with an enhanced performance.

Keywords: Frictional heating; hip implants; temperature rise

1. Introduction

Total hip replacement (THR) is one of the successful advanced and sophisticated medical surgeries in the world, which replaces natural hip with arthritis by artificial components, bringing back its normal functions to patients. Due to the nature of structure and function of the implant, heat generation and transfer phenomenon continually occurs within the THR system. Studies show that a significant amount of heat is generated, which may severely affect the performance of the implant. The heat generation can be due to (1) the bone-cement-implant polymerization for the fixation of the stem and the cup (in the case of cemented implants), (2) cutting and drilling of the bone during orthopedic surgery, and (3) frictional sliding at the articulating interface between the head and the cup. While the formers are attempted by many researchers to understand and model the mechanism [1-5], the temperature increase due to the latter is found to be significant and poses a critical threat to the life of implants as well as patients. This is the focus of the present paper. The amount of frictional heat generated is a function of several factors including speed and duration of the joint movement, applied load, quality of lubricant, articulating materials (i.e. thermal properties), and the presence of wear or other debris [6, 7]. It can also found to be a function of the implant design and the quality of the bearing components incorporated. These have rigorously been realized by researchers through *in vivo* measurements, *in vitro* tests, and computational modeling techniques [e.g., 8, 9]. The overall conclusion is that frictional heating causes temperature rise on the order of about 1-10°C, and the bearing materials with low friction are being recommended, to some extent, to suppress frictional heating. It is recognized that the potential for heating is most applicable for heavier, more active patients under an extended period of activities. Studies, however, unanimously stress the possible concerns with such frictional heating. High temperature generated in the joint capsule, not only causes degradation of the bearing component, particularly soft UHMWPE (ultra high molecular weight polyethylene) cup, but also increases the risk of damage to the surrounding biological tissues. Even excessive temperature increase may deteriorate the lubrication property and further elevate wear generation at the interface. As a result of these is the failure of the implant and the need for revision surgery within a shorter period of time. Over the decades, tremendous efforts have been put forward to understand and address the above issues associated with frictional heating, and to answer a question about how to reduce its impacts. In light of this quest, this paper aims to review frictional heating in hip implants across the

literature, particularly focusing on its mechanism and estimation techniques. While various factors impacting frictional heating are discussed, concerns and potential remedies are addressed.

2. Quantification of heat generation

In order to better appreciate its mechanism and quantification, the frictional heating at the interface is attempted by researchers through a number of approaches. The following sections review some of those investigations.

2.1. In vivo measurements

In an *in vivo* investigation, Bergmann et al. [8] studied temperature and joint forces of five patients with seven instrumented hip implants with alumina ceramic head against the UHMWPE cup using telemetry transmission data. The details of the temperature measurements can be found in [10]. By measuring the temperature directly from the implants rather than the synovial fluid, they showed that the maximum temperature in the femoral head reaches to 41°C after one hour of walking, and varies significantly with the patients. The temperature of the synovial fluid is also found to be 2-3°C higher than that in the femoral head. Walking is shown to generate higher temperature than cycling. The findings also outline the detrimental effect of frictional heat (e.g. degradation of biological tissues) on the stability of the hip implants. Very recently, by placing temperature sensors in the articulating components made of different material combinations, J.W. Pritchett [11] extensively studied resurfaced hips of 12 patients (12-36 months after hip resurfacing procedure) where the synovial temperatures are recorded after patients walked for 20-60 minutes. While the heat generated is documented to vary significantly with material combinations, resurfaced hips generate more heat than the arthritic and normal hips, and arthritic hips generate more than normal hips. The temperature rises from the base line (temperature) with respect to time, type of hips, patients, and the bearing materials studied are illustrated in Table 1. Other factors such as patient size, activity type, and activity level, which can also result in the temperature variation, are not considered in this study. It seems intuitive that the young, more active patients with jogging cycle would generate more heat within the joints. Further, in *in vivo* studies, a larger amount of observations with a greater number of patients for a longer period of monitoring (i.e. time period after hip replacements) would be necessary to take into consideration in order to comprehensively depict that the amount of heat generation is clinically relevant to the implant's life or its function.

Table 1. Synovial fluid temperature rise across patient and implant type during walking cycle, reproduced with permission from [11].

Patient	**R Hip**	**L Hip**	**Baseline R/L (°C)**	**20min R/L (°C)**	**60min R/L (°C)**
1	Normal	Metal hemi	36/37	1/2	2/4
2	Metal-on-metal	Degenerative joint diseases	39/37	8/2	8/3
3	Ceramic hemi	Normal	38/37	1/1	3/2
4	Degenerative joint diseases	Metal-on-polyurethylene	37/38	2/5	3/6
5	Ceramic-on-polyurethylene	Ceramic-on-metal	38/38	5/5	5/4
6	Metal-on-metal	Metal-on-metal	38/38	8/8	8/8
7	Ceramic-on-PEEK	Ceramic-on-PEEK	37/37	4/4	4/4

R: Right, L: Left, Baseline: Initial temperature within the joint

2.2 In vitro tests

While *in vivo* measurements are quite expensive and, sometimes, nearly impossible to conduct, *in vitro* tests are a practical way to evaluate the equivalent clinical performance of the hip system. Using hip simulators equipped with thermal sensors on the laboratory setup, researchers widely studied thermo-mechanical characteristics in terms of temperature rise and its effects on frictional torque, material wear and strength [e.g., 7, 12]. An equivalent joint motion and lubrication is employed, which closely represents an *in vivo* situation. Effects of materials, loading magnitude, sliding frequency and surface roughness on the temperature distribution in/at the bearing surface are extensively investigated [7, 12, 13]. Some aspects of them will be detailed in Section 3. For example, Lu and McKellop [12] reported that, after the equilibrium state, the maximum temperature occurs at the load axis point of the UHMWPE cup surface and varies as 35.6±3.8, 40.4±1.8, and

51.3±5.2°C for the articulating head of alumina, Co-Cr and zirconia, respectively (the room temperature is of 22°C). Other studies in [e.g., 7] found slightly lower temperatures. The reciprocal-sliding of the Co-Cr-Mo head against the UHMWPE cup in phosphate buffered saline as lubricant shows that the equilibrium contact temperature (maximum) increases up to 12°C in 30 minutes under contact pressure of 12.7 MPa and sliding speed of 50 mm/s [13]. By undertaking wear tests in the sterile filtered bovine calf serum as a lubricant, Rocchi et al. [14] showed that for the UHMWPE cup articulating against the Co-Cr head, the maximum temperature in the cup and the lubricant is about 47.97±3.79 and 42.5°C respectively, which is higher than that obtained from Davidson et al. and Lu and McKellop's studies. This would be due to wider range of loading, test protocols, types of lubricants, temperature measurement system, and thermal properties of the bearing materials used in the studies. The precipitation of the proteins in the lubricants is found to follow the rank of the temperature rise for bearing combinations investigated.

While the temperature rises measured are lower than the precipitation threshold value (of about 60°C) [15], under higher loading and sliding speed, substantially higher bearing temperature and hence, greater amount of protein precipitation may be expected. This, consequently, will degrade the boundary lubrication property of the protein, mechanical properties of the bearing materials (e.g. soft UHMWPE), and wear resistance of the bearing surface. This is more likely to happen for the zirconia head against UHMWPE cup as the equilibrium temperature of the lubricant and the bearing component is relatively higher. In [6], the authors performed the so-called "simulated *in vivo*" tests where the joint movement is replaced by the resistance heater embedded in the femoral head, and the system is assembled in such a way as to resemble the actual situation as much as possible. In the tests, the joint capsule is simulated by pieces of bovine muscle tissue to reproduce the *in vivo* environment; however, the effect of vascularity and blood flow is not reproduced in such setup. Another concern with in-vitro studies is that heating the lubricant in the test chamber up to 37°C to replicate the *in vivo* one may cause potential overheating of the bearing material, and weakens its property as well. A more anatomical orientation of the cup rather than the cup is positioned facing up against head is also emphasized [12]. A standard hip simulator test protocol pertaining proper environment and condition which are close to those of the *in vivo* is hence needed to further improve the accuracy of the laboratory based wear tests.

2.3 Computational modeling

As the frictional heating is a local effect in the bearing component, sometimes it is quite difficult for measuring instruments to locate the highest temperature point. Further, setup of sensors (e.g., thermocouples) needs drilling holes, which may impact overall heat transfer and measurement. Therefore, along with *in vivo* and *in vitro* studies, as an alternative, computational modeling of frictional heating is extensively studied by researchers across the world. In this approach, researchers adopt analytical, semi-analytical, and numerical analysis techniques. As integrated, implemented, and tested in other environments, the approach is found to be an effective and fast way to predict and analyze the behavior of the system [12, 16-19]. Thermo-mechanical coupled mechanism is used in all the analyses since it is recognized that the heat generated by the friction is the result of combined effect of heat and mechanical deformation within the system. This means that the temperature rise causes deformation and change contact condition in articulating bodies. The mathematical description of the mechanism is detailed in [e.g., 17]. Using 2 and 3-D finite element (FE) modeling, researchers estimated the steady and transient temperature distribution in the bearing components, and compared with those obtained from hip simulator/clinical studies [12, 14, 17]. The estimated temperature in the UHMWPE cup surface studied across the literature is always found to be higher than the measured one by on the order of 6-7°C or sometimes, even more. The modeling considers thermal equilibrium of the system where the heat generation rate by friction equals the heat dissipation rate. The time to reach such equilibrium state is found to vary. Using different head materials against the UHMWPE cup, Zu and McKellop [12] and Rocchi et al. [14] reported that the maximum temperature at the contact area of the cup surface reaches after about 6-7 hours. Suhendra and Stachowiak [18] suggested that, with a small friction at the interface, the maximum temperature reaches after about 2 hours. I*n vivo*, however, this occurs in a shorter period (of about one hour) of walking [8].

While computational modeling can reasonably simulate the overall behavior, the accuracy of the technique is largely limited by a number of factors. For example, oversimplification of physiological loading mechanism and anatomical orientation of actual hip model are just few of them. Effect of temperature on the wear, lubrication, and change in material properties (e.g. Young's modulus) that would naturally happen in the *in vivo* environments are rarely simultaneously considered and replicated in the available models. Another important issue is that the correct choice of important parameters to be employed in the model depends on the experiments. For example, the heat generation rate at the interface, thermal properties of bearing materials, surrounding tissues and synovial fluid must be obtained accurately from the experiments. This needs to be addressed because, as is already shown in [8], the experimental results widely scatter. In addition,

modeling of the change of properties of tissues and bearing materials with temperature and integrating it into the solution package (e.g., FE method) is yet to be a growing challenge to realize the actual phenomena. So it is imperative that the fully validated computational modeling which will mimic *in vivo* condition needs to be developed for the accurate estimation of frictional heating. This, in turn, can be used as a benchmark tool to do parametric study for the evaluation of bearing component with discovery of new material and design.

3. Factors affecting frictional heating

With the *in vivo*, *in vitro*, and computation modeling techniques, researchers extensively investigated effects of different parameters on frictional heat generation. This section briefly outlines some findings.

3.1. Effect of bearing material and joint load

Bearing material has a remarkable influence on heat production, wear, and friction. By studying different pair of bearing materials (i.e. head-on-cup order) in *in vitro* studies, Davidson et al. [6, 7] concluded that alumina-on-alumina generate the least heat as compared to the alumina-on-UHMWPE, Co-Cr alloy-on-UHMWPE couples (see Fig. 1). This is because the alumina has the highest thermal conductivity and the least frictional coefficient among its counterparts. During the tests, an equivalent gait cycle (i.e. load-time history) is selected to reflect natural hip loading during walking while two peak loads, P_{max} of 2500N and 5000N are applied through the femoral head. As can be seen in Fig. 1, the level of joint load affects the maximum temperature. Similar results of the temperature variation are also observed by other studies [11, 12, 18]. This indicates that new bearing materials with improved thermal properties (e.g. high thermal conductivity) are needed to be discovered and applied in the implants. Due to its excellent mechanical and biological properties, PCD (polycrystalline diamond) is becoming a potential option and currently being used as the bearing material [20, 21].

3.2. Effect of frictional coefficient

With FE modeling of steady state and transient heat transport, Suhendra and Stachowiak [18] and Hu et al. [17] studied the effect of friction at the interface on the heat generation. As shown in Fig. 2, the higher frictional coefficient generates the greater amount of heat, and hence results in higher temperature gradient. While after some period of time (i.e. equilibrium point), the effect of friction is negligible. Hence improving the surface finish of the articulating components is important to minimize friction and thus, heat generation. The more details of the interaction between the friction coefficient, contact pressure, and temperature rise for the Co-Cr-on-UHMWPE couple investigated through laboratory based tests can be found in [13].

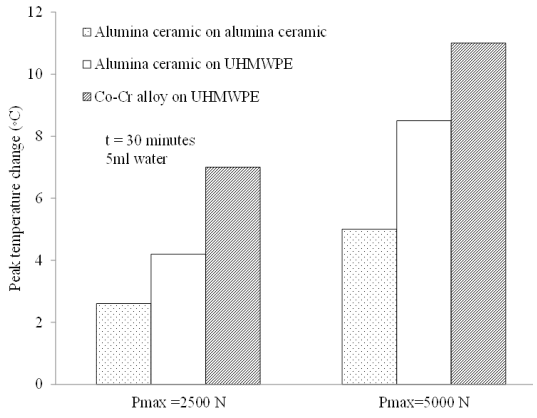

Fig. 1. Change in temperature rise in the UHMWPE cup with friction, reproduced with permission from [18]

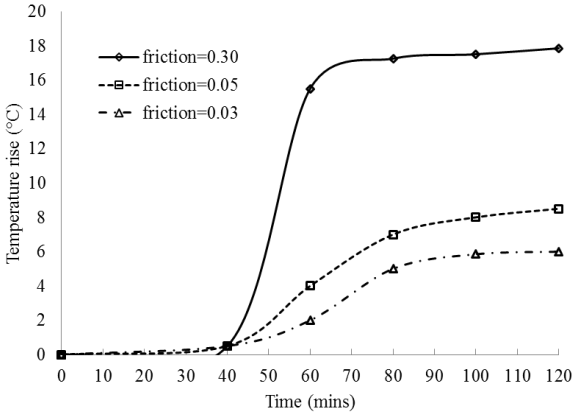

Fig. 2. Change in temperature rise in the UHMWPE cup with friction, reproduced with permission from [18]

3.3. Effect of sliding speed

Suhendra and Stachowiak [18] examined the effect of sliding speed (i.e., the relative motion between the head and the cup during either hip or sliding wear tests) on the temperature rise. As can be depicted from Fig. 3, the sliding speed has a significant effect on the surface temperature. During 15 minutes of sliding, the difference in maximum temperature reached at the higher (13.4228 rad/s) and the lower (1.3423 rad/s) sliding speeds is about 7°C. From FE simulations under given gait load and rotational angle, Hu et al. [17] also concluded higher heat generation and greater temperature gradient with the increase of the sliding speed. This outlines an obvious influence of the frequency of sliding between the head and the cup due to abnormal activities on the heat generation. This would be more severe, particularly, for active, young, and sporty patients.

3.4. Effect of lubrication

Lubrication is another important factor affecting friction, frictional torque, wear, and heat generation. The synovial fluid, a biological substance within the joint capsule amounting on the order of $2cm^3$ (in volume), acts a lubricant to smooth out relative motion between the bearing components. It forms a film layer of a small thickness ranging from 6µm to 1mm depending on the type of the joint and location. In addition to providing hydrodynamic boundary lubrication, it offers necessary nutrients for the cartilage and protects it from the enzyme activity, thus retaining the healthy state of the joint capsule. In an *in vitro* test, Davidson et al. [7] studied lubrication effects using water and/or hyaluronic acid for different material combinations. Friction in dry medium and in the presence of 2 mg bone cement powder is investigated as well. They conclude that, for a given material pair, water and hyaluronic lubrication provide lower frictional torque and has a negligible influence with each other, while friction in dry medium, as can be predicted, is significantly higher. Figure 4 shows a representative result of the relationship between the lubrication and the frictional torque observed for ceramic-on-UHMWPE pair [7]. It is, however, addressed that because of low viscosity and hyaluronic acid content in implants, mixed lubrication, and hence, accelerated frictional heating is expected to occur *in vivo*.

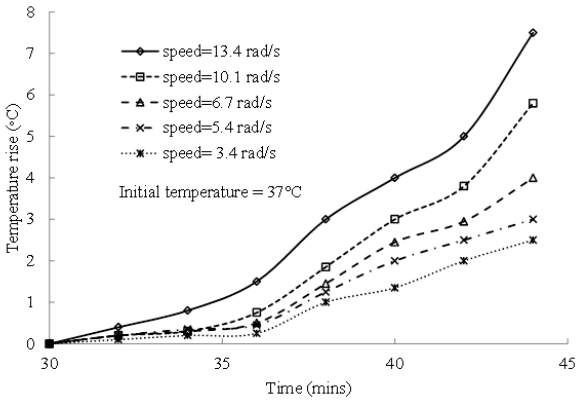

Fig. 3. Change in temperature rise in the UHMWPE cup with the sliding speed, reproduced with permission from [18]

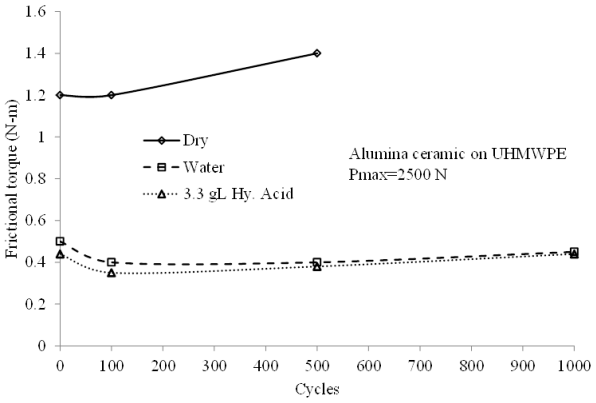

Fig. 4. Change in frictional torque with lubrication condition within the joint, reproduced with permission from [7]

4. Concerns and possible solutions

Past studies clearly demonstrate that even the best bearing components experience temperature rise due to frictional heating, particularly during extended period of joint activity (i.e. gait loading). Depending on material, loading, and activity period, such temperature rise in the synovial fluid and the bearing components can reach up to on the order of 50°C and 56°C or even more, respectively. While thermal precipitation forms a thin solid layer, protecting bearing surfaces from wear, excessive precipitation due to greater frictional heating degrades the lubrication property, thus accelerating the adhesive wear between surfaces. This can be further favoured by the flash-heating or frictional shearing of proteins [22]. Other *in vivo* risks associated are creep and oxidation degradation of the soft UHMWPE as well as potential severe damage to the surrounding biological tissues and bone. It has been reported that a temperature rise of a little as 6°C can cause cell death, fibrous tissue formation, and possibly periprosthetic pain; all of which will eventually lead to the aseptic loosening failure [e.g., 23, 24]. While frictional heating is obvious, initiatives in terms of development of new bearing material, processing of materials, improved design and surgical procedure are urgently to be sought to minimize its aforementioned

impacts. For example, in an *in vitro* investigation, Y.S. Liao et al. [15] suggested that circulating a coolant at an appropriate temperature within the femoral head can reduce remarkably the bearing temperature rise and prevent excessive protein precipitation, while retaining wear surfaces and morphologies closely comparable to those *in vivo*. A recent work further proposes that by promoting graphitic layer on metal-on-metal couples is likely to reduce wear, friction, and corrosion [22]. Graphene-UHMWPE composite is potentially a new bearing material and shown to offer an excellent wear resistance and low friction as compared to standard UHMWPE [25]. The mechanism of frictional heating is a vital phenomenon, and, thus, needs to be addressed and taken into careful consideration in the future design and implementation in order to be able to ensure an improved stability and longevity of implants.

5. Conclusions

A comprehensive review of frictional heating in hip implants is presented in this paper. It is clear that depending on bearing material, joint load, and activity period, the temperature rise would be sufficiently high to cause degradation of materials and lubrication properties, which result in an instability and/or aseptic loosening failure of implants. While reasonably accurate, the approaches such as *in vitro* and computational modelling techniques need to be improved with appropriate guidelines obtained from the experiments to better appreciate and quantify the heat generation *in vivo*. The above necessitates that biomedical engineers, material scientists, and clinical surgeons must work closely to devise new solutions to overcome the issue associated with frictional heating and hence, to extend the life of implants.

References

[1] Hansen E. Modelling heat transfer in a bone-cement-prosthesis system. J Biomech 2003; 36:787-795.
[2] Mathew LS and Hirsch C. Temperatures measured in human cortical bone when drilling. J Bone Joint Surg Am 1972; 54/2:297-308.
[3] Mazzullo S, Paolini M, Verdi C. Numerical simulation of thermal bone necrosis during cementation of femoral prostheses. J Math Bio1991; 29/5:475-494.
[4] Stanczyk M and Telega JJ. Thermal problems in artificial joints: influence of bone cement polymerization. Acta Bio-Eng Biomech 2001; 3/2: 489-496.
[5] Kaorapapapong K and Amornsamankul S, Tang IM, Wisatangapataphee B. Heat transfer in cemented hip replacement process. Int J Mechcs 2011; 5/3: 202-209.
[6] Davidson JA, Gir S, and Paul JP. Heat transfer analysis of frictional heat dissipation during articulation of femoral implants. J Biomed Mat Res: App Biomat 1988; 22/A3:281-309.
[7] Davidson JA, Schwartz G, Lynch G, Gir S. Wear, creep, and frictional heating of femoral implant articulating surfaces and the effect on the long-term performance, Part II: friction, heating and torque. J Biomed Mat Res 1988; 22:69-91.
[8] Bergman G., Graicen F., Rohlmann A., Verdonschot N., Van Lenthe G.H., Frictional heating of total hip implants, Part 1: measurements in patients, J Biomech 2001; 34/4: 421-428.
[9] Bergmann G, Graicen F, Rohlmann A, Verdonschot N, Van Lenthe GH. Frictional heating of total hip implants, Part 2: finite element study. J Biomech 2001; 34/4: 429-435.
[10] Graichen F, Bergmann G, and Rohlmann A. Hip endoprothesis for in vivo measurement of joint force and temperature. J Biomech 1999; 32/10:1113-1117.
[11] Pritchett, JW. Heat generated by resurfacing prostheses: An in vivo pilot study. J Long-Term Eff Med Imp 2011; 21/1:55-62.
[12] Lu Z and MacKellop H. Frictional heating of bearing materials tested in a hip joint wear simulator. J Eng Med 1997; 121:101-108.
[13] Imado K, Miura A, Nagatoshi M, Kido Y, Miyagawa H, and Higaki H. A study on contact temperature due to frictional heating of UHMWPE. Trib Lett 2004; 16/4: 265-273.
[14] Rocchi M, Affatato S, Falasco F, and Viceconti M. Thermo-mechanical analysis of ultra-high molecular weight polyethylene-metal hip prostheses. J Eng Med 2007; 221: 561-568.
[15] Liao YS, McKellop H, Lu Z, Campbell P, and Benya P. The effect of frictional heating and forced cooling of the serum lubricant and wear of UHMWPE polyethylene cups against cobalt-chromium and zirconia balls. Biomat 2003; 24: 3047-3059.
[16] Fialho JC, Fernandes PR, Eca I, and Folgado J. Computational hip joint simulator for wear and heat generation. J Biomech 2007; 40: 2358-2366.
[17] Hu CC, Liau JJ, Lung CY, Huang CH, and Cheng CK. A two-dimensional finite element model for frictional heating analysis of total hip prostheses. Mater Sc Eng C 2001; 17:11-18.

[18] Suhendra N and Stachowiak GW. Temperature prediction in a finite element model for sliding contact analysis of total hip prosthesis. J Eng Med 2004; 218:361-370.
[19] Sawyer WG, Hamilton MA, B.J. Fregly, S.A Banks. Temperature modelling in a total knee joint replacement using patient specific kinematics. Trib Lett 2003;15/4:343-351.
[20] Uddin MS and Zhang LC. Contact stresses in PCD-on-PCD hip joint prostheses. Int Conf Adv Trend Eng Mat App; 4-8 July 2011, Milan Italy.
[21] Chen Y, Zhang LC, Arsecularatne J and Montross C. Polishing of polycrystalline diamond by the technique of dynamic friction, part 1: prediction of the interface temperature rise. Int J Mach Tools Manuf 2006; 46(6): 580–587.
[22] Liao Y et al. Graphitic tribological layers in metal-on-metal hip replacements. Science 2011; 334:1687-1690.
[23] Oosterveld FG, and Rasker JJ, Effects of local heat and cold treatment on surface and articular temperature of arthritic knees. Arthritis Rheum 1994; 37: 1578-82.
[24] Ericsson AR and Alnrektsson T. Temperature threshold levels for heat induced bone injury: a vital-microscopic study in the rabbit. J Pros Dental 1983; 50: 101-107.
[25] Chen Y, Qi Y, Tai Z, Yan X, Zhu F, and Xue Q, Preparation, mechanical properties and biocompatibility of grapheme oxide/ultrahigh molecular weight polyethylene composites. Euro Ploy J 2012; 48: 1026-1033.

Available online at www.sciencedirect.com

SciVerse ScienceDirect

Procedia Engineering 00 (2012) 000–000

Procedia Engineering

www.elsevier.com/locate/procedia

5th BSME International Conference on Thermal Engineering

The Properties of Copper (I) Iodide (CuI) Thin Films Prepared by Mister Atomizer at Different Doping Concentration

M.N. Amalina[a,*], Y. Azilawati[a], N.A. Rasheid[a], M. Rusop[a,b,*]

[a]*NANO-ElecTronic Centre (NET), Faculty of Electrical Engineering, Universiti Teknologi MARA, 40450 Shah Alam, Malaysia*
[b]*NANO-SciTech Centre (NST), Faculty of Applied Science, Universiti Teknologi MARA, 40450 Shah Alam, Malaysia*
[c]*Faculty of Applied Science, Universiti Teknologi MARA, 40450 Shah Alam, Malaysia*

Abstract

In this paper, we present the properties of CuI thin films at different concentration of iodine doping. Mister atomizer technique or so called spray pyrolysis has been applied to deposit CuI thin films on the glass substrate at a constant deposition parameter. The effects of iodine concentration to its surface morphology, electrical and optical properties were studied. The physical characteristics of sprayed CuI were determined by field emission scanning electron microscopy (FESEM), current voltage (I-V) measurement and UV-VIS-NIR spectrophotometer. A uniform thin films with nanoparticle sized of CuI was observed for all deposited samples. The resistivity shows a parabolic pattern where 3at% of iodine doping has the highest resistivity of 1.03 x 10^3 Ω cm. The transmittance for all samples was transparent of above 70% in the visible wavelength. The transmittance and absorption coefficient was measured and then the energy gap was determined which shows the direct transition of n=2. The maximum band gap observed here is 2.73 eV at 3 at% of doping concentration. The 3at% of iodine doping shows the highest resistivity, less transmittance and high band gap was due to the surface morphology and surface traps create by iodine doping.

Keywords: copper (I) iodide; mister atomizer; iodine doping; electrical properties; optical properties

Nomenclature

CuI	Copper (I) iodide
at%	Atomic percent
α	Absorption coefficient (m)
$h\nu$	Photon energy (m)
Eg	Energy band gap (eV)

1. Introduction

Copper (I) iodide is a wide band gap semiconductor with three crystalline phases which are α, β, γ. The low temperature of γ-CuI which is below 350˚C with a cubic structure was chosen since it behaves as a p-type semiconductor with a large band gap of 3.1eV. The uppermost valence band of CuI ($\Gamma_{15,2}$ and $\Gamma_{12,1}$) are derived from 3d states of Cu and 5p states of iodine.

* Corresponding author. Tel.: +603-5543-1883
E-mail address: amalina.muhamad@gmail.com, rusop@salam.uitm.edu.my

The energy difference between $\Gamma_{15,\ 2}$ and $\Gamma_{12,\ 1}$valleys at Γ point in the Brillouin zone was 3.1eV which define its direct fundamental bandgap [1]. CuI has attracted much interest because of its unique features such as larger band gaps, a negative spin orbit splitting [2], an unusually large temperature dependency, electrosensivity [3], an anomalous diamagnetism behavior, new high pressure phases [4], and photosensivity [5]. The γ- CuI has potential application in light emitting diode due to large exciton binding energy (62 meV) which will caused a high intensity of violet emission [6]. Besides that, another possible applications of CuI are field emission display, organic catalyst, solid state dye sensitized solar cell as a hole conductor and etc [7-9]. Several techniques have been reportes by the literature for the preparation of γ-nanostructured CuI films such as by simple complex compund method [10], ethanol thermal method [11], pulse laser deposition [1] and etc.

In this paper, we highlighted a new approach for depositing CuI (inorganic compound) thin films using the spraying technique with a system called as mister atomizer. Spraying technique is a simple and inexpensive, however able to give high production rates. The iodide material had not yet been explored extensively and most commonly used precursors for spraying technique for an inorganic compound are nitrate, carbonate, sulfate and chloride [12]. In spraying technique, the intended product may be achieved by optimizing the solution properties such as the precursor concentration, doping composition or variation of solvent used. Here, the iodine doping concentration was varied to observe its effect on the opto-electrical properties. The surface morphology, electrical and optical properties of the CuI thin films deposited by mister atomizer at different iodine doping concentration was discussed.

2. Experimental Procedure

2.1. Sample Preparation

Glass substrates of 2.5cm x 2.5 cm were used for the CuI deposition. The cleaning process of glass substrates was done by using acetone, methanol and deionized water in the ultrasonic cleaner stage by stage at 10 minutes each. The deposition of CuI films were taken at room temperature by atomization technique. Spraying technique which carried by our own experimental setup called as mister atomizer was used for the deposition of CuI thin films. Mist-atomisation is a process similarly known as spray pyrolysis. The process involves spraying precursor solution onto heated surface and the constituents react to form the intended products [13]. The mister atomizer utilizes the concept of pressure atomization which its generation mechanism is using shear force by expansion of pressurized liquid [12]. Principally, the droplets of liquid are produced applying inertial force on liquid stream. The solution molarity was fixed at 0.05M CuI solution by mixing precursor Copper (I) Iodide powder (ALDRICH, 98%) with acetonitrile as a solvent. All chemicals were used without any further purification. The iodine which act as dopant were varied at 1 at%, 2 at%, 3 at%, 4 at% and 5 at%. The atomic percent (at%) concentration were calculated as shown in equation (1):

$$y\ at\% = \frac{a}{a + 0.05}\ x\ 100$$

Where *a* is the molar concentration of dopant and 0.05 is the molar concentration of CuI.

The undoped and doped CuI solutions were stirred for 3 hours at room ambient condition . Before the deposition , the substrates were preheated at 50℃ in the furnace before the deposition process. This solution was then sprayed in fine droplets using argon as a carrier gas. The solution volume was 50 ml for all samples. Then the films were heated for about 5 min in the furnace after completed the deposition process to evaporate the solvent. In order to get uniform thin films, the flow rate, solution molarity, height between substrate and nozzle were kept constant during the deposition.

2.2 Characterization technique

The characterization carried in this experiment is the surface morphology, electrical and optical properties. The thickness of the thin films has been characterized by using surface profiler (VEECO DEKTAK 150). The surface morphology of these CuI films was observed by field emission scanning electron microscope (JEOL JSM- J600F). The current-voltage measurement of CuI thin films in dark condition and under illumination were measured by solar simulator (CEP 2000). Gold was used as metal contacts for I-V measurement and deposited using sputter coater (EMITECH K550X). The optical transmittance for undoped and iodine doped CuI thin films were characterized by JASCO UV-VIS-NIR spectrophotometer. The uncoated glass slide was used as the reference sample. The wavelength for the optical measurement was measured at wavelengths between 300 nm- 800 nm. All of the measurements were done in room ambient.

3. Results and Discussion

3.1. Surface Morphology

The result of CuI films thickness for undoped and doped is graphically represented in Fig. 1. It was found that the CuI films thickness decreased with increasing iodine concentration. The highest thickness was obtained for undoped film of about 553 nm. Figure 2(a) – 2 (f) shows the FESEM images of CuI films at different doping concentration. The FESEM images reveal all the films are uniformly deposited with nanoparticle CuI. It is observed that there is not much difference in terms of particle size for all the prepared samples. However, the roughnesses of the samples were slightly different especially at higher doping concentration. The 5 at% iodine doping concentration shows the roughest surface with agglomerated CuI particle was clearly seen compared to others. It can be seen that roughness of the thin films increases with increasing I_2 concentration. This phenomenon may be attributed to the increase of surface undulation of the thin films as I_2 concentration increases [14]. Besides roughness, the thin films deposited at 3 at% and 5 at% shows a crack formation on the thin films. Higher crack was seen for thin film deposited at 3at% of iodine concentration. The crack morphology certainly affects the resistivity value and will be discussed detailed in the electrical properties part.

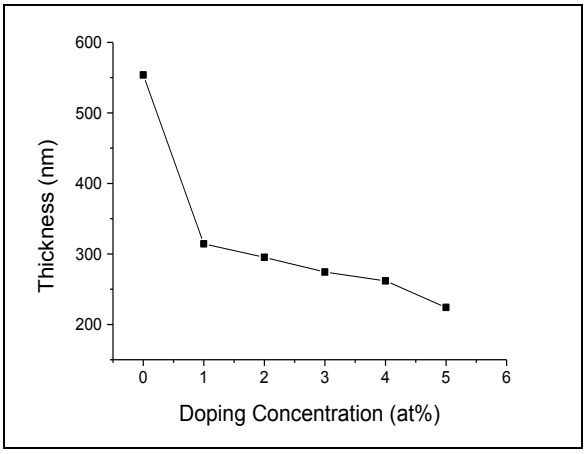

Fig. 1. Thickness of CuI films at different iodine doping concentration

3.2 Electrical Properties

The electrical properties of semiconductor materials are highly affected by the doping process. Fig. 3 shows the plot of resistivity for undoped and iodine doped CuI films at 1 at% to 5 at%. The I-V measurements were done with two different measurements ambient which are in dark and illumination condition. The illumination was carried out by using white light bias of 100 mW/cm^2. The CuI thin films show almost no photo response since no different was seen when compared with measurement carried in dark condition. The small electron carrier in the p-type CuI compared to holes carrier leads to less photo response properties as shown in the Fig. 3. The photo response characteristic is very important for the n-type semiconductor especially for the application of solar cells. For both measurement conditions, a parabolic behavior with an optimum peak is observed. It can be clearly seen that, the resistivity increased from 4.75 Ω cm for undoped thin films to an optimum peak of 1.03 x 10^3 Ω cm for films prepared with at 3 at% doping concentration.

This shows that the resistivity reaches a maximum peak at 3 at% I_2 doping. The p-type conductivity of CuI depends on the excess of iodine in the stoichiometric excess. Therefore, iodine doping can be either increased or decreased the resistivity which corresponds to the position of surface traps induced by iodine in the band position of CuI. Presumably, the resistivity increases as the I_2 ions increases is due to the interstitial I_2 atoms in the lattice that act as a charge trapping of electrons. The surface traps in the lattice which created by excess of iodine not just encourage the recombination process to occur but at the same time reducing the carrier mobility. Perera et. al reported that the surface trapping sites is 0.2 eV above the valence band of CuI [9]. The 3 at% shows the highest resistivity which caused by the crack formation on the thin film as shown in Fig. 2. The crack films will increase the scattering of carrier and thus exhibit less electron movement. The reduction of resistivity for 4 at% and 5 at% may be due to the reduce grain boundaries which lead to better carrier mobility at higher doping concentration condition.

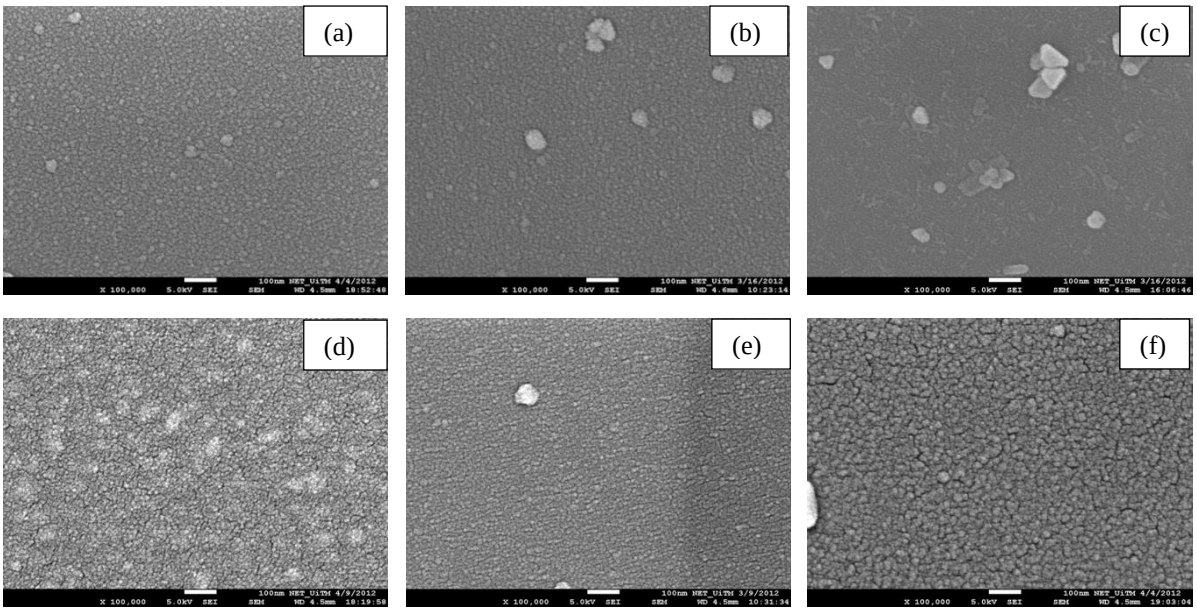

Fig. 2. FESEM images of CuI thin films for (a) undoped, (b) 1 at%, (c) 2 at%, (d) 3 at%, (e) 4 at%, (f) 5 at%

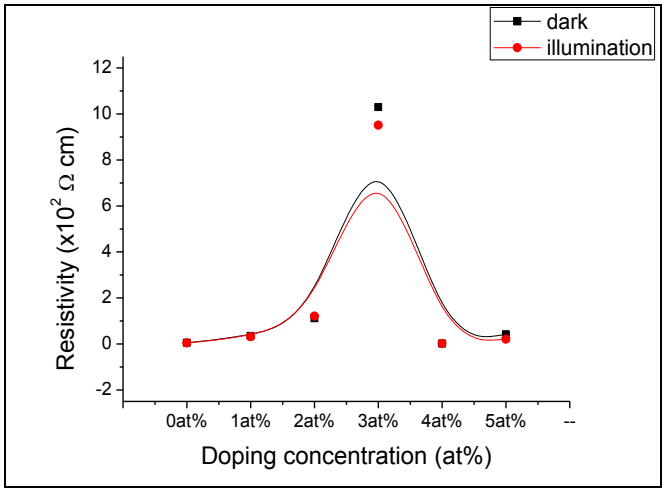

Fig. 3. Resistivity of CuI films at different iodine doping concentration in dark and under illumination condition

3.3 Optical Properties

The optical transmission spectra of CuI thin films prepared on glass substrate at different doping concentrations are shown in Fig. 4 (a) and (b). The two graphs were plotted for transmittance spectra in this research paper are because to emphasize the graphs so that it can be clearly seen. All films exhibit high transparency in the visible range between 400– 800 nm of the optical spectrum. The observed hump at 410 nm may be due to excitation of electrons from sub bands in the valence band to the conduction band [1]. The decrease of transmittance up to 3at % may be attributed to the increased scattering of photons by crystal defects created by doping [15]. This is proved by the electrical properties as shown in Fig. 3 where the resistivity increased up until 3 at% of doping concentration. The transmittance increased after 4 at% of I_2 doping which parallel to the resistivity value.

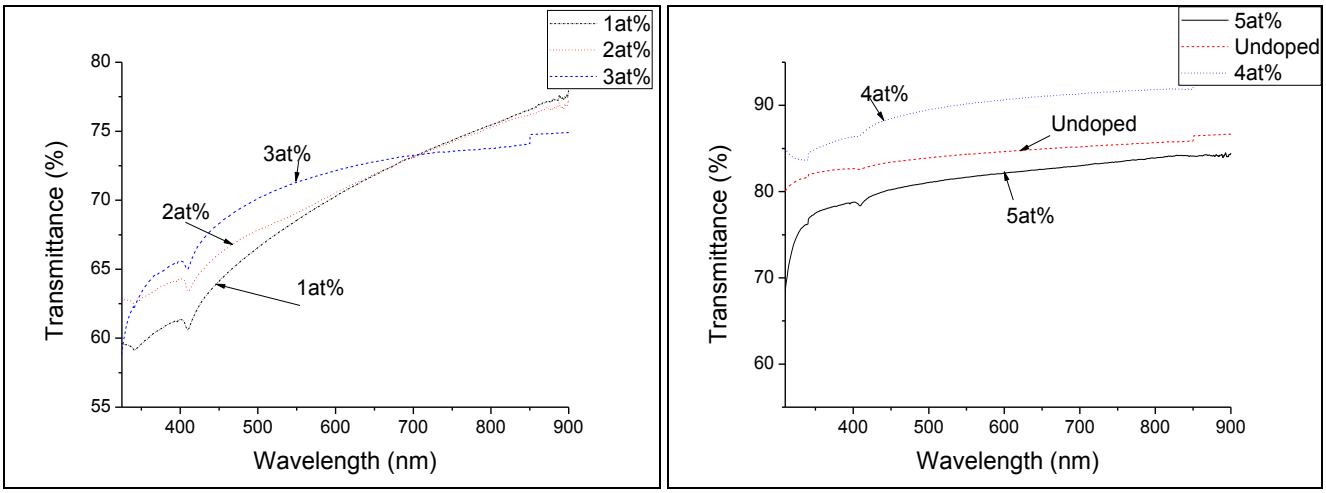

Fig. 4 Transmittance spectra of CuI films at (a) 1 at%, 2 at % and 3 at% (b) undoped, 4 at% and 5 at%

The transmittance analysis in the locality of the fundamental absorption edge shows the variation of absorption coefficient, α with photon energy (*hv*) is in accordance to the following relation which implies direct band transition as shown in Eqn [1]:

$$\alpha hv = A\,(\,hv - Eg)^{1/2} \tag{1}$$

where α is the absorption coefficient, *A* is a constant, *hv* is the photon energy, *Eg* is the bandgap.

The band-gap energy E_g of doped CuI thin films for different doping concentration was summarized in Table 1. It shows that the band gap widens with increasing I_2 doping concentration up to 3 at%. The direct band gaps of CuI film prepared by mister atomizer increased between 2.6 eV to 2.72 eV and gradually decreased to 2.53 eV for I_2 concentration of 5 at%. The optical band gap obtained here is parallel to the resistivity value where 3 at% of doping showed the highest resistivity with higher band gap. The broadening effect can be understood based on the Burstein effect, which implies an increase in the Fermi level in the conduction band of semiconductors leading to widening of the optical band-gap [16]. The increasing Fermi level in the conduction band is due to increased carriers in the films.

The values obtained in this research work of below 3.1 eV were also obtained by other authors [17]. However, the reported band gap of CuI by Sekkal et al. is 3.1eV [18]. The lower band gap compared to 3.1 eV helps in better utilization of the blue region of the solar spectrum which means at longer wavelength of visible spectrum.

TABLE I
BANDGAP ENERGY OF CUI FILM AT DIFFERENT I_2 DOPING CONCENTRATION

Atomic percent (at%)	Band gap (ev)
Undoped	2.60
1 at%	2.64
2 at%	2.66
3 at%	2.73
4 at%	2.59
5 at%	2.53

Conclusion

I_2 doped CuI thin films have been successfully deposited by mister atomizer under constant deposition flow rate. The thickness was found to be decreased as the doping concentration increased with undoped CuI thin film having the highest thickness of 553 nm. The good quality of the deposited thin film had been shown by its morphology, electrical and optical properties. From the FESEM images, uniform thin films were obtained by using mister atomizer with nanoparticle size of CuI. However, at 3 at% of doping, small crack formation was seen on the films. This is proved by resistivity value where 3 at% of concentration show the highest resistivity of 1.03 x 10^3 Ω cm. The high resistivity value obtained is due to the surface trap states induced by excess of iodine. The transmittance spectra of undoped and doped CuI films show high

transmittance of above 70% in the visible range. The optical band gap increases with doping concentration from 2.60 eV to 2.73 eV for the doping concentration increase from undoped films to 3 at% doping concentration. The optimization of doping concentration for thin film properties is owing to the suitable resistivity, transmittance and optical band gap dependence on the required application.

Acknowledgements

Many thanks to Universiti Tekonologi Mara (UiTM), Ministry of Higher Education (MOHE) and Research Management Institute (Excellence Fund (600-RMI/ST/DANA 5/3/Dst (397/2011)), UiTM for the financial support

References

[1] P. M. Sirimanne, M. Rusop, T. Shirata, T. Soga, and T. Jimbo, "Characterization of transparent conducting CuI thin films prepared by pulse laser deposition technique," *Chemical Physics Letters*, vol. 366, pp. 485-489, 2002.
[2] M. Cardona, "Optical properties of the silver and cuprous halides," *Physics Review*, vol. 129, pp. 69-78, 1963.
[3] S.F. Lin, W.E. Spicer, and R. S. Bauer, "Temperature-dependent photoemission studies of the electronic states of CuBr," *Physics Review B*, vol. 14, p. 4551, 1976.
[4] H. Feraoun, H. Aourag, and M. Certier, "Theoretical studies of substoichiometric CuI," *Material Chemical Physics*
vol. 82, pp. 597-601, 2003.
[5] D. Chen, Y. Wang, Z. Lin, J. Huang, X. Chen, D. Pan, and F. Huang, "Growth strategy and physical properties of the high mobility p-type cui crystal," *Crystal Growth and Design*, vol. 10, pp. 2057-2060.
[6] A. Gruzintsev and W. Zagorodnev, "Effect of annealing on the luminescence of p-CuI crystals," *Semiconductors*, vol. 46, pp. 149-154, 2011.
[7] J.-H. Lee, D.-S. Leem, and J.-J. Kim, "High performance top-emitting organic light-emitting diodes with copper iodide-doped hole injection layer," *Organic Electronics*, vol. 9, pp. 805-808, 2008.
[8] P. M. Sirimanne, T. Soga, and T. Jimbo, "Identification of various luminescence centers in CuI films by cathodoluminescence technique," *Journal of Luminescence*, vol. 105, pp. 105-109, 2003.
[9] V. P. S. Perera and K. Tennakone, "Recombination processes in dye-sensitized solid-state solar cells with CuI as the hole collector," *Solar Energy Materials and Solar Cells*, vol. 79, pp. 249-255, 2003.
[10] Y. Zhou, M. lÃ¼, G. Zhou, S. Wang, and S. Wang, "Preparation and photoluminescence of Î³-CuI nanoparticles," *Materials Letters*, vol. 60, pp. 2184-2186, 2006.
[11] Y. Liu, J. Zhan, J. Zeng, Y. Qian, K. Tang, and W. Yu, "Ethanolthermal synthesis to Î³-CuI nanocrystals at low temperature," *Journal of Materials Science Letters*, vol. 20, pp. 1865-1867, 2001.
[12] D. Jung, S. Park, and Y. Kang, "Design of particles by spray pyrolysis and recent progress in its application," *Korean Journal of Chemical Engineering*, vol. 27, pp. 1621-1645, 2010.
[13] J. B. Mooney and S. B. Radding, "Spray Pyrolysis Processing," *Annual Review of Materials Science*, vol. 12, pp. 81-101, 1982.
[14] J. Lu, K. Huang, J. Zhu, X. Chen, X. Song, and Z. Sun, "Preparation and characterization of Na-doped ZnO thin films by solâ€“gel method," *Physica B: Condensed Matter*, vol. 405, pp. 3167-3171.
[15] C. M. Muiva, T. S. Sathiaraj, and K. Maabong, "Effect of doping concentration on the properties of aluminium doped zinc oxide thin films prepared by spray pyrolysis for transparent electrode applications," *Ceramics International*, vol. 37, pp. 555-560, 2011.
[16] Z. B. Achour, T. Ktari, B. Ouertani, O. Touayar, B. Bessais, and J. B. Brahim, "Effect of doping level and spray time on zinc oxide thin films produced by spray pyrolysis for transparent electrodes applications," *Sensors and Actuators A: Physical*, vol. 134, pp. 447-451, 2007.
[17] Y. Yan, S. Zhou, Z. Lu, and Z. Li, "Microstructure and optical properties of sprayed γ-CuI thin films for CuInS solar cells," *Rare Metals*, vol. 30, pp. 22-27.
[18] W. Sekkal and A. Zaoui, "Monte Carlo study of transport properties in copper halides," *Physica B: Condensed Matter*, vol. 315, pp. 201-209, 2002.

Available online at www.sciencedirect.com

SciVerse ScienceDirect

Procedia Engineering 00 (2012) 000–000

Procedia Engineering

www.elsevier.com/locate/procedia

5th BSME International Conference on Thermal Engineering

Chemical Solution Deposited Magnesium Oxide Films: Influence of Deposition Time on Electrical and Structural Properties

Z. Habibah[a,b,*], A. N. Arshad[c], L. N. Ismail[a], R. A. Bakar[a], M. Rusop[a,b,*]

[a]*NANO-ElecTronic Centre (NET), Faculty of Electrical Engineering, Universiti Teknologi MARA, 40450 Shah Alam, Malaysia*
[b]*NANO-SciTech Centre (NST), Faculty of Applied Science, Universiti Teknologi MARA, 40450 Shah Alam, Malaysia*
[c]*Faculty of Applied Science, Universiti Teknologi MARA, 40450 Shah Alam, Malaysia*

Abstract

Magnesium oxide thin films have been deposited on glass substrate using simple chemical solution technique. Film thickness was varied (171, 238, and 506nm) by controlling the deposition time. The electrical behaviour of MgO films showed leakage current density below 10^{-7} A/cm^2 for voltage range from -10V to 10V. Resistivity value of the film was found to be increased due to the large grain boundary produced in the film. The formation of island like structure was detected at film thickness of 506 nm which composed of nanoparticle MgO. The 238nm film was found to be suitable thickness of dielectric layer due it electrical properties and structural properties which include resistivity, leakage current density, roughness and particle size respectively.

Keywords: Magnesium oxide; Thickness; Chemical deposition; Electrical properties; Structural properties

Nomenclature

MgO	Magnesium oxide
t_{ox}	Thickness
ρ	Resistivity (Ω.cm)
J	Current density (A.cm^{-2})

1. Introduction

Metal oxides have attracted attention for many applications such as in sensors, RF devices, optoelectronic, plasma display panel (PDP) and as insulating layer [1-3]. Among these materials, Magnesium oxide is a good candidate to be used as insulating material due to its wide bandgap (~7.8eV), high dielectric constant (~9), high breakdown field and have merits of good chemical and thermal stability [4, 5]. High oxygen affinity and low temperature of Mg cause this compound easy to synthesis and suitable to growth on various substrates [2]. Moreover, because of its higher Poisson's ratio and lower Gibb's free energy, it have been used as template for ferroelectrics [6] and as buffer layer between semiconductor and oxide material [7]. MgO thin films can be deposited using several techniques such as vacuum evaporation, sputter deposition, chemical vapor deposition and chemical deposition. Chemical depositions include spray pyrolysis and spin coating techniques [8]. However, deposition of thin film using sol-gel method has its own advantages such as high purity, large area coating, stoichiometry control, simple and it also cost effective. The thickness played significant roles towards electrical and

* Corresponding author. Tel.: +603-5543-1883
E-mail address: habibahzulkefle@yahoo.com, rusop@salam.uitm.edu.my

optical properties of the films [9-11]. Besides, structural properties which include surface roughness and morphology of the film also influence by the film thickness [12]. Therefore this paper reported on the effect of the MgO film thickness to it electrical and structural properties by varying the deposition time via simple chemical method.

2. Experimental Procedure

2.1. Solution and Films Preparation

Magnesium acetate tetrahydrate was dissolved in ethanol with small addition of nitric acid to be act as the stabilizer. The solution was then sonicated in ultrasonic bath at 50°C for 20 minutes. Heating, ageing and stirring processes were then carried out at 80°C and room temperature respectively. Prepared solution was then deposited on the glass substrate via spin coating method with the parameter were set to 3200 rpm for 30 sec and followed by drying process. These processes were repeated at several times (5, 10, and 15 times) to achieve three different film thicknesses. Finally the deposited MgO films were annealed at 500ºC for 1 hour in chamber furnace.

2.2. Films Characterizations

The electrical characterization was performed using two point probes I-V measurement (BUKOH-KEIKI) with gold as the metal contact for the prepared films. Thickness, t_{ox} of deposited films was measured by surface profiler (Veeco) while for structural properties, atomic force microscopy (AFM-Park System XE100) and field electron scanning emission microscopy (FESEM-JEOL JSM 7600) were used to determine the surface topography and morphology of prepared MgO films respectively.

3. Results and Discussion

3.1. Effect on Electrical Properties

The electrical properties of deposited MgO films were observed in terms of current voltage (*I-V*) behavior, resistivity and leakage current density. Fig. 1a shows the *I-V* characteristic of the films where the current was linearly increased with applied voltage. From the slope of the *I-V* graph, the values of resistance for each film was determined and by using the following equation (Eq. 1) the resistivity of the films are obtained.

$$\rho = \frac{w t_{ox}}{l} R \tag{2}$$

where ρ is the resistivity, R is the resistance, w is the width, t_{ox} is the thickness and l is the length. As can be seen in Fig. 1b, the resistivity value was increased as the thickness of MgO film increased. The resistivity of MgO film at thickness of 171 nm and 238 nm are 12.69×10^4 and 19.39×10^4 Ω.cm respectively. However, when the film thickness reached 506 nm the resistivity value drastically increased to 68.89×10^4 Ω.cm. Resistivity value obtained in this work is quite similar with work done by S. Lee et al. which their resistivity value is ~10^4 Ω.cm [13] . Increased in resistivity was due to the large grain boundary area produced in the film. Therefore the carrier transport and carrier mobility in the film is reduced [13, 14]. This was proven by the FESEM images (Fig. 5) where the inhomogeneous film produced as the thickness increased from 171 nm to 506nm. Besides based on the resistivity formula (Eq. 1), resistivity is films thickness dependence; therefore rise in resistivity was also due to the thicker film of MgO.

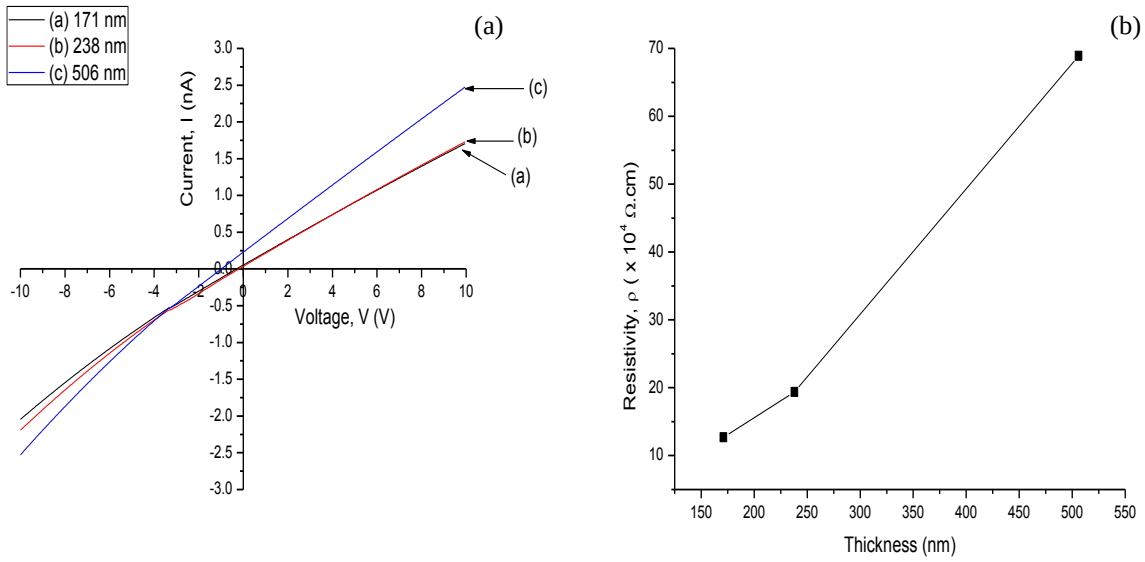

Fig. 1. Electrical behaviour in terms of (a) *I-V* characteristic and (b) Resistivity for deposited MgO films.

Leakage current density, *J* is one of important criteria in determining the best dielectric film. High dielectric material with low current density will lead to produce high dielectric strength material. C.Bondoux et al. also investigate current leakage density of MgO films and they found that the current density was two order of magnitude lower (10^{-6} A/cm^2) [5] than common insulator layer (SiO_2 ~4 x 10^{-4} A/cm^2) . Leakage current density (Fig. 2) of deposited MgO films in this work was found to be three orders of magnitude (1x10^{-7} A/cm^2) lower than SiO_2 over the voltage range of -10 to 10V and it has same in magnitude with T. L. Chen et. al [15]. From the graph also, it shows that as the thickness increased the leakage current also increased. Somnath et al. also found the same trend in their MIM capacitor [16]. We expected that this was related to the porosity formed in the film which created a path for the carrier to pass through the film.

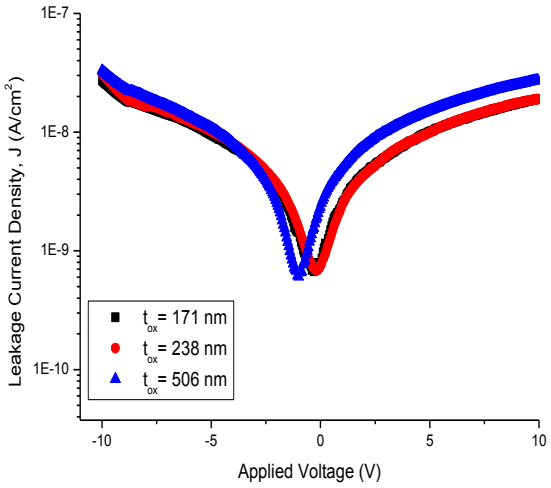

Fig. 2. Leakage current density, *J* at various MgO thicknesses measured at room temperature.

3.2. Effects on Surface Topography and Morphology

Surface topography in 3-dimensional images of deposited MgO films observed by AFM was shown in Fig. 3. As stated by G. Hu et al. surface roughness of the films was the measure of the surface texture of the film in terms of their RMS value

of the surface height profile of the film [17]. From the images and RMS surface roughness data tabulated in Table 1, it revealed that the roughness of the film decreased from 29.049 nm to 18.942 nm when the film thickness increased from 171 nm to 238 nm. This was due to the small particle produced in MgO film with 238 nm thickness. However, it can be seen that the film roughness was then increased to 202.396 nm when the film thickness reached 506nm. K.K. Nanda et al. stated that the roughness of the film was determined by the difference between peak and valley on the film surface [12]. Since this film was in island structure form (Fig. 5a), therefore the difference between peak and valley is higher and lead to the higher surface roughness [13].

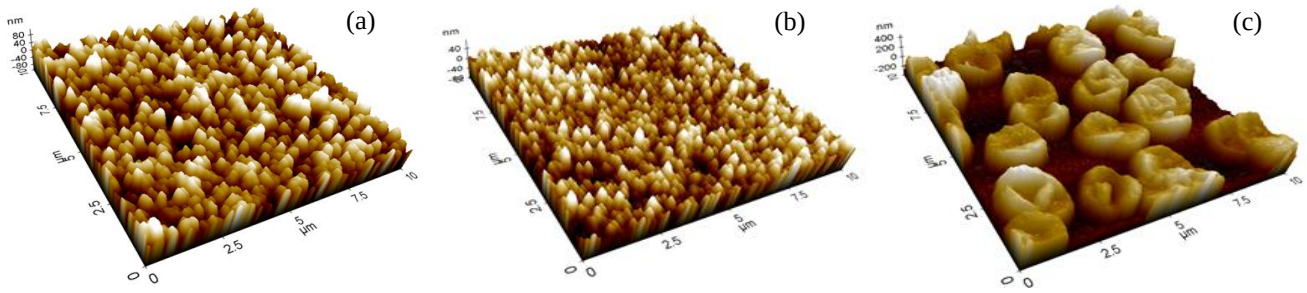

Fig. 3. Surface topography with thickness (a) 171nm, (b) 238nm and (c) 506nm of deposited MgO film.

Table 1. Influence of thickness on the surface roughness of MgO films.

Thickness of MgO Films (nm)	Root Mean Square Roughness, Rq (nm)	Average Surface Roughness, Ra (nm)
171	29.049	23.228
238	18.942	14.981
506	202.396	180.465

FESEM images in Fig. 4 shows the surface morphology of MgO film at thickness of 171-506 nm at 50k magnification. It shows that, the morphology of the film was thickness dependence where the grain boundary of the film became larger as the thickness increased. From the surface morphology obtained, it clearly being seen that as the thickness of the film increased from 171 nm to 238 nm, the size of the MgO particles are reduced. Nevertheless, the number of voids in the film was higher compared to film with 171 nm.

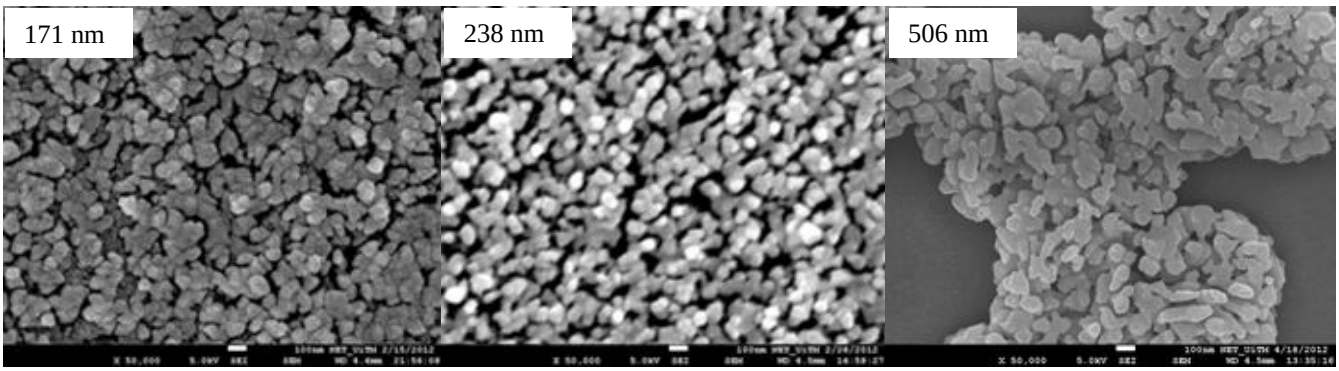

Fig. 4. FESEM images of magnesium oxide thin films at 50K magnification at different thickness.

As stated by W. Xu et al. higher growth film will contribute to the formation of high density film with porous structure [18]. The morphologies obtained were similar to those reported in S. K. Shukla et al. [8] and S. H. Tamboli et al. [9] where MgO particles are in nanometer dimension with some porosity in their films. We also found that, at thickness of 506 nm, the film produced was in island structure and it being proven by surface morphology of the film presented in Fig. 5 (a). This was due to the large increment in the thickness [4]. Evolution of film is divided into two stages which are initial nucleation and agglomerated grain [4, 19]. Therefore, it can be said that, below 506 nm, the film growth was in nucleation state and became a seed layer to produce island structure and the large grain composed of nanometer particle of MgO (Fig. 5b). In order to investigate the elements existing in the deposited MgO films, Energy Dispersive Spectrometer (EDS) analysis (Fig. 5c) have been performed and it confirms the presence of magnesium and oxygen elements in the films with some contamination of sodium. Besides, platinum peak also observed and this was due to the coating process during the analysis.

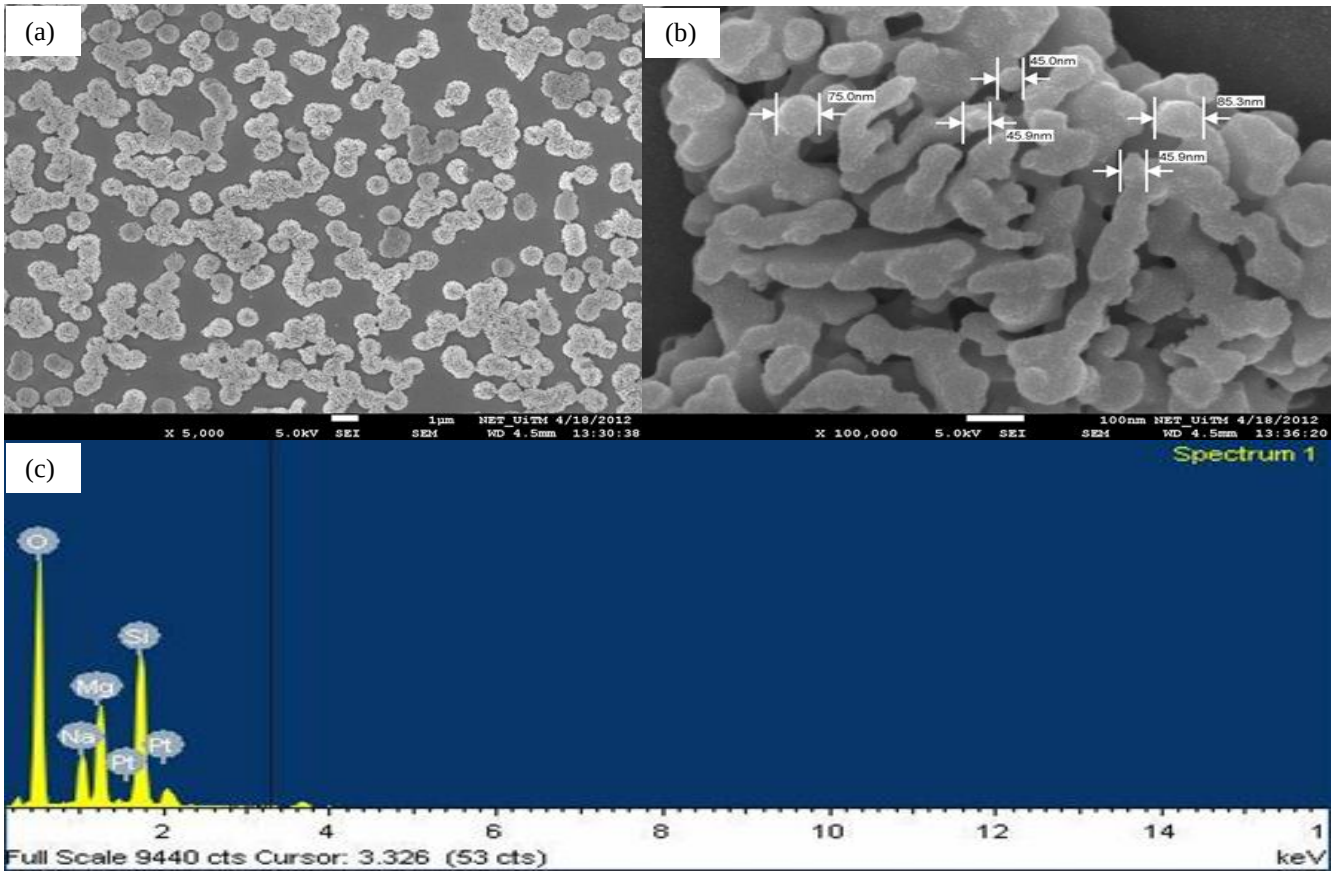

Fig. 5. Surface morphology at magnification of (a) 5k, (b) 100k and (c) EDS spectra of 506 nm MgO film.

Conclusion

Magnesium oxide, MgO film with different thickness (171, 238 and 506nm) has been successfully deposited on glass substrate using simple chemical deposition technique by controlling the deposition time. Electrical properties obtained revealed that as the thickness increase, the insulating characteristic of the film are reduced where the leakage current density, *J* was increased. However, the obtained leakage current density value (10^{-7} A/cm^2) was smaller than SiO_2 which is suitable to be used as dielectric layer. Increased in grain boundaries resulted in the reduction of resistivity value of the deposited films which caused by high carrier scattering. Island structure composed of MgO nano particle was observed for film with 506nm thickness. MgO film with 238 nm thickness was suitable to be used as dielectrics because of high resistivity and low leakage current density. In addition, the particle size produced in this film was in nanometer dimension which will enhance the surface area per unit volume of the film.

Acknowledgements

The authors would like to thanks Ministry of Higher Education (MOHE), Malaysia and Research Management Institute, RMI of Universiti Teknologi MARA for providing financial support under grant Dana Kecemerlangan 600-RMI/ST/DANA 5/3/Dst (401/2011).

References

[1] T. Abukawa, S. Sato, and Y. Matsuoka, Surface Science 604 (2010), 1614.
[2] S. Benedetti, H. M. Benia, N. Nilius, S. Valeri, and H. J. Freund, Chemical Physics Letters 430 (2006), 330.
[3] D. S. E. Atanassova, Microelectronic Reliability 42 (2002), 1171.
[4] V. P. Shital Patil, Microelectronics International 29 (2012), 3.
[5] P. P. C. Bondoux, P. Belleville, F. Guillet, R. Jerisian, Material Science Forum 457-460 (2004), 1373.
[6] A. M. E. Raj, M. Jayachandran, and C. Sanjeeviraja, "Fabrication techniques and material properties of dielectric MgO thin films--A status review," *CIRP Journal of Manufacturing Science and Technology*, vol. 2, pp. 92-113, 2010.
[7] Y. J. K. HJong-Gul Yoon, Journal of the Korean Physical Society 31 (1997), 613.
[8] S. K. Shukla, G. K. Parashar, A. P. Mishra, P. Misra, B. C. Yadav, R. K. Shukla, L. M. Bali, and G. C. Dubey, Sensors and Actuators B: Chemical. 98 (2004), 5.
[9] S. H. Tamboli, V. Puri, and R. K. Puri, Applied Surface Science 256 (2010), 4582.
[10] J. Lee, T. Jeong, S. Yu, S. Jin, J. Heo, W. Yi, D. Jeon, and J. M. Kim, Applied Surface Science 174 (2001), 62.
[11] P. N. A. James R. Groves, Harriet Kung, Stephen R. Foltyn, Raymond F. DePaula, Luke A. Emmert, IEEE Transactions on Applied Superconductivity 11 (2001), 2822.
[12] S. N. S. K. K. Nanda, S. N. Sahu, Applied Surface Science 133 (1998), 293.
[13] S. Lee and T. Ito, Materials Research Bulletin 40 (2005), 951.
[14] J. Li, J.-H. Huang, W.-J. Song, Y.-L. Zhang, R.-Q. Tan, and Y. Yang, Journal of Crystal Growth 314 (2011), 136.
[15] X. M. L. T. L. Chen, X. Zhang, Applied Physics A: Materials Science & Processing 79 (2004), 1857.
[16] T.-M. P. Somnath Mondal, IEEE Device Letters 32 (2011), 1576.
[17] G. Hu, G. Orkoulas, and P. D. Christofides, Chemical Engineering Science 64 (2009), 3903.
[18] W. Xu, B. Li, T. Fujimoto, and I. Kojima, Surface and Coatings Technology 135 (2001), 274.
[19] K. C. Chenggang Zhuang, Joan M. Redwing, Qi Li, X X Xi, Superconductor Science and Technolog, 23 (2010).

Available online at www.sciencedirect.com

SciVerse ScienceDirect

Procedia Engineering 00 (2012) 000–000

Procedia Engineering

www.elsevier.com/locate/procedia

5th BSME International Conference on Thermal Engineering

Fabrication and Characterization of Camphor-based Amorphous Carbon Thin Films

A.N. Fadzilah[a,b], K. Dayana[a], M. Rusop[a,b]

[a]Nano-ElecTronic Centre (NET), Faculty of Electrical Engineering,
[b]Nano-SciTech Centre (NST), Institute of Science,
Universiti Teknologi Mara (UiTM),
40450 Shah Alam, Selangor, Malaysia

Abstract

Pure amorphous carbon (a-C) and nitrogen doped amorphous carbon (a-C: N) thin films were prepared using Thermal Chemical Vapor Deposition (CVD) with deposition temperature ranging from 500^0C to 650^0C using camphor ($C_{10}H_{16}O$) as a precursor from natural source. The physical and optical properties of deposited a-C and a-C: N thin films were characterized by UV-Vis-NIR spectroscope and Raman spectroscope. The presence of 2 peaks known as Raman D peaks and Raman G peaks ensure the amorphous structure of carbon (C). Raman I_D/I_G ratio for both pure and nitrogen doped a-C as deposition temperature increase indicates more graphitic structure in high temperature of a-C and a-C: N. Highest transmittance indicated at thin film with lowest deposition temperature (500^oC) and vice versa. At visible range (390 nm to 790 nm) the transmittance exhibit high transmittance of above 80% at low temperature (500 and 550). However, at high temperature (600 and 650) transmittance is low (30% - 70%). The absorption coefficient, α for both a-C and a-C: N is reported to be ~x10^5 cm^{-1}. From Tauc's plot, optical band gap (E_g) was determined and E_g found to decrease as deposition temperature increased from 0.2 to 0.9 eV for pure a-C and 0.2 to 0.75 eV for nitrogen doped a-C.

Keywords: Amorphous carbon; Nitrogen doped; Thermal CVD; Raman spectroscope; Optical properties

Nomenclature

CVD	chemical vapour deposition
a-C	amorphous carbon
a-C:N	nitrogen doped amorphous carbon
FWHM	full width at half-maximum
I_D/I_G	ratio of D-peak intensity to G-peak intensity
α	absorption coefficient

1. Introduction

Amorphous carbon (a-C) consists of diamond like sp^3 and graphite like sp^2 carbon bonding ratio thus possess excellent mechanical such as superior hardness and excellent wear resistance [1]. a-C has low friction coefficients and provides protection for the counter parts [2] thus is suitable not only for typical mechanical applications such as in protective coating, wear resistant coating and antireflective coating but for optical application as well [3]. Amorphous carbon (a-C) has semiconducting nature which is able to accept dopants [4], wide band gap from 0.0 eV to 5.5 eV [5] and tunable band gap by adjusting the sp^2 and sp^3 of carbon bonding ratio[6] by doping techniques on the a-C thin films which is weakly p-type in nature. To the best of our knowledge, the properties of a-C are strongly dependent on the deposition condition such as the deposition temperature. Carbon films which consist of varying proportion of sp^3 and sp^2 bonded in a-C can be obtained. For

* Corresponding author. Tel.: +603-55441883
E-mail address: nurfadzilahahmad@yahoo.com

the case of a-C with sp^3-coordinated carbon, it has four in-plane σ bonds whereas for a-C with sp^2-coordinated carbon, it has three σ bonds and one π bonds. Between the filled bonding state (σ and π) and empty anti bonding state (σ* and π*), the photon assisted electronic transition occurred [7]. Since the π state is localized it has inconsistent bond between any other allotrope in a-C. π state also has weaker bond and lies closer to Fermi level (E_f) than the σ state. Thus π states form the valence band edge and π* states form the conduction band edge thus clarify that the π and π* controlled the optical gap size. So by controlling the sp^2 and sp^3 ratio, the properties of a-C is controllable.

Nitrogen doped amorphous carbon (n-C:N) is reported as a conductive material for electrical analysis. Several advantages include a low background current, a large potential window and inertness in chemically aggressive environments [8]. In pursuit of producing high electrical conductivity of a-C, doping was introduced. Nitrogen (N) incorporated a-C shows better electrical conductivity and high photoconductivity [9]. Raman spectroscopy is one way to determine the structural and phase disorder information of the a-C [10]. The first order of Raman spectra is a single sharp line at about 1332 cm^{-1} for diamond and at 1350 cm^{-1} for defective graphite (D peak). The main peak centered at 1580 cm^{-1} indicates the monocrystalline graphite (G peak). In this paper the Raman scattering studies on pure a-C and a-C: N were studied to understand the structural properties and improvement of a-C when doping is introduced, supported by optical investigation by UV-vis-Nir spectroscope.

2. Methods

The properties of carbon films depend not only to the deposition condition but the starting precursor as well. For various kinds of deposition process, graphite target is commonly used for the preparation of carbon-based materials. However camphor ($C_{10}H_{16}O$) which consists both sp^2 and sp^3 carbon is an attracting new material for carbon-based preparation since graphite has only sp^2 carbon. Pure amorphous carbon (a-C) and nitrogen doped amorphous carbon (a-C: N) thin films were prepared using Thermal Chemical Vapor Deposition (CVD) system. The system consists of a cylindrical quartz tube inside a 2 furnace system CVD to create a deposition environment for the a-C. Camphor oil was chosen as the precursor and Argon (Ar) gas and Nitrogen (N_2) gas as the carrier gas and dopant gas respectively on a well cleaned corning glass.

The glass substrates have been cleaned in acetone (C_3H_6O) followed by methanol (CH_3OH) for 10 min respectively using an ultrasonic cleaner (Power Sonic 405) to eliminate contaminations. Finally the substrate was blow with nitrogen gas (N_2). The precursor was placed at furnace one and substrate was hold horizontal inside furnace two. In order to ensure the cleanliness of the quartz tube before the deposition process starts, the quartz tube was purged with Ar gas for 15 minutes. Temperature of the furnace two was elevated from room temperature to desired deposition temperature (500^0C to 650^0C) under argon atmosphere whereas furnace one is kept constant at 200^0C. Deposition process was carried out for 30 minutes and for doping process, the Ar gas was replaced by N_2 gas. The flow rate was set at 30 bubbles /minute with the gas pressure 213 Bar/3062 Psi. For structural and optical characteristic, Raman spectroscope and Perkin Elmer Lambda 750 UV-vis-NIR spectroscope were used for the characterization process.

3. Results and Discussion

Raman spectra were investigated by Raman spectroscope at room temperature and the samples were scanned in the range of 1000 to 1800 cm^{-1} for pure a-C and a-C:N deposited from 500-650^{o}C. Due to the structural sensitivity, Raman analysis is widely used for the analysis of carbon and carbon related materials such as the amorphous carbon. Figs. 2 and 3 displayed the Raman shift for a-C and a-C: N respectively, using the same scale. Two asymmetric peaks at around 1350 cm^{-1} and 1590 cm^{-1} were obtained for both cases which are typical for a-C as reported by others [11-15]. Raman peak at 1590 cm^{-1} is known as G-peak and corresponds to the active mode in mono-crystalline graphite while for Raman peak at 1350 cm^{-1} known as D-peak is related to the disorder in the carbon which appears in microcrystalline or defective graphite. The G-peak appears from the Raman allowing the E_{2g} mode and the D-peak results from grain boundary effect [15]. The G-mode also involves the in-plane bond stretching vibration of any pair of sp^2 whereas the D-peak is A_{1g} symmetry involves the sp^2 inside the ring only [16]. In other words, D-band is said to correspond to the defects associated with the vacancies and the presence of other carbonaceous impurities that destroys the graphitic symmetry of the G-band [17, 18].

The peak position, the full width at half-maximum (FWHM) and the integrated intensity ratio of the two peaks (I_D/I_G) are obtained from the Gaussian fittings. As can be seen from Figs. 1 and 2, the samples have increasing intensity as temperature increases and gradually grow splitter. From both graphs for Raman spectra, it was indicated that the increase in intensity is due to increase in thickness (45 to 84 nm for undoped and 40 to 70 nm for nitrogen doped) of the films [11]. For undoped samples, D-peak position starts from 1363 cm^{-1} at 500^{o}C and moves slightly to the lower wave number up to 1355 cm^{-1} at 650^{o}C. On the other hand, the G-peak shifts to higher wave number from 1568 to 1592 cm^{-1} and becomes narrower as the temperature increases (FWHM decrease). The D-peak however becomes wider as temperature increases (FWHM increase). As can be seen, at temperature 600^{o}C the G-peak FWHM is the narrowest (83.30 cm^{-1}) and this indicates the

* Corresponding author. Tel.: +603-55441883
E-mail address: nurfadzilahahmad@yahoo.com

increase of crystallinity and graphitization in the C-C phase of the deposited films, similar to the DLC and CNT films [19, 20].

For doped samples, D-peak position starts from 1368 cm^{-1} at 500^{o}C and moves slightly to the lower wave number up to 1350 cm^{-1} at 650^{o}C. However for the G-peak of a-C: N the position does not appear to follow the same trend as pure a-C and it roughly keeps on the same position at ~1592-1596 cm^{-1} while the intensity increases. The behaviour has proven the increased of sp^2 carbon bonding as temperature increases [21]. Beeman et al. [22] in the theoretical model of a-C explains that the raman G-peak position is the measure of sp^2 fraction of carbon bonding and will be downshifted with increasing sp^3 fraction of carbon bonding. The broad band structure of the films suggests the amorphous behaviour of the films. The same trend of FWHM follows in the a-C: N where G-peak becomes narrower as the temperature increased (FWHM decrease – 75.89 cm^{-1}) and vice versa for the D-peak up to 600^{o}C. As for the higher temperature of 650^{o}C in both undoped and nitrogen doped cases, the FWHM of the G-peak becomes slightly wider and this might be due to the increasing in defect structure. Details on the Raman value were tabulated in tables 1 and 2 for numerical comparison.

From the two Gaussian peaks, the Raman I_D/I_G ratio was calculated as shown in tables 1 and 2 for pure a-C and a-C: N respectively. For pure a-C, the I_D/I_G ratio reduces from 0.86 to 0.70 (deposition temperature 450^{o}C to 600^{o}C) but rose slightly to 0.76 when deposition temperature is higher, 650^{o}C. The same tendency was observed at a-C: N with the highest I_D/I_G ratio is 0.82 and reduced to 0.66 at 600^{o}C. However, the I_D/I_G ratio increases to 0.73 at 650^{o}C. Lowest I_D/I_G ratio at 600^{o}C is an evidence for high crystallinity of a-C [23] together with lowest FHWM of G-peak as discussed before. Thus it is concluded that lower I_D/I_G ratio when N doping was introduced is due to the graphitization of a-C. The deposition rate was derived from the ratio of the film thickness to the deposition time (30 mins) by averaging the thickness measured for five times using surface profiler at different locations. For both undoped and doped samples, the deposition rate increase as deposition temperature increase, which was from 1.33 to 2.8 nm/min for undoped and 1.03 to 2.5 nm/min for nitrogen doped a-C. The increase in the deposition rate is attributed to the higher deposition temperature where the thickness increases.

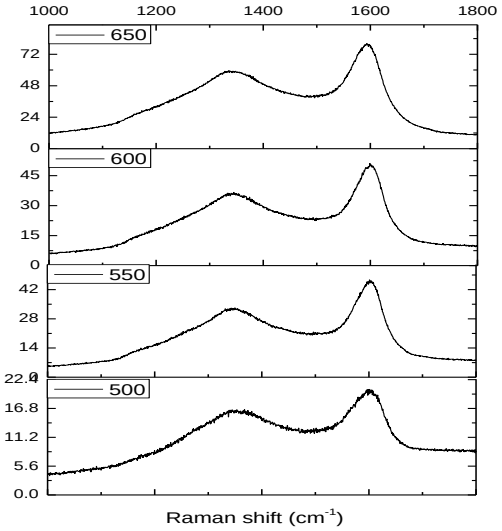

Fig 1. Raman shift for pure a-C

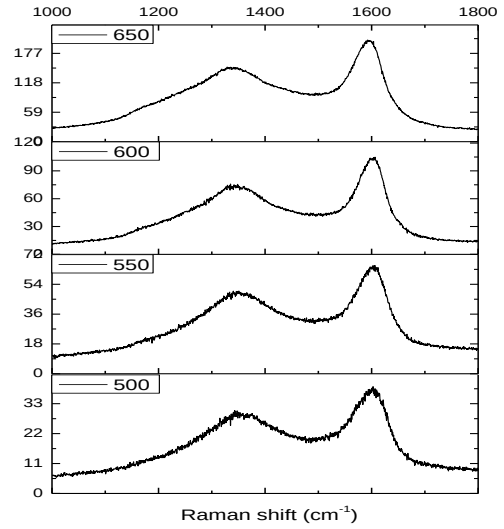

Fig 2. Raman shift for a-C:N

Table 1. Details on Raman value for pure a-C

Deposition temperature (^{o}C)	D position (cm^{-1})	D FWHM (cm^{-1})	G positin (cm^{-1})	G FWHM (cm^{-1})	I_D/I_G ratio	Rate (nm/min)
500	1363	217.88	1569	122.56	0.83	1.50
550	1356	257.02	1597	84.52	0.77	2.10
600	1358	269.99	1596	83.30	0.70	2.33
650	1355	313.90	1592	84.06	0.78	2.80

* Corresponding author. Tel.: +603-55441883
E-mail address: nurfadzilahahmad@yahoo.com

Table 2. Details on Raman value for a-C:N

Deposition temperature (°C)	D position (cm^{-1})	D FWHM (cm^{-1})	G position (cm^{-1})	G FWHM (cm^{-1})	I_D/I_G ratio	Rate (nm/min)
500	1368	238.70	1596	93.50	0.73	1.33
550	1365	238.40	1598	88.41	0.71	1.83
600	1356	259.38	1598	75.89	0.66	2.00
650	1350	291.39	1592	80.85	0.73	2.50

The optical properties were investigated by a Perkin Elmer LAMBDA 750 UV-vis-NIR spectroscope measurement for the a-C thin films deposited on the quartz substrates. Figs. 3(a) and (b) show the optical transmittance versus wavelength of the a-C thin films deposited at different deposition temperatures for pure a-C and a-C:N. It is observed that in both undoped and doped cases, the optical transmittance had a high value (>80%) at the visible range 3 (1.56 to 3.18 eV) for 500°C and 550°C. At 600°C and 650°C, the transmittance reduces to 60% and 40% respectively. However, a-C: N has slightly higher transmittance compared to pure a-C. The high transmittance could be explained to be related to the reduction of the sp^2 phase in the film, which absorbs the visible wavelength range [24].

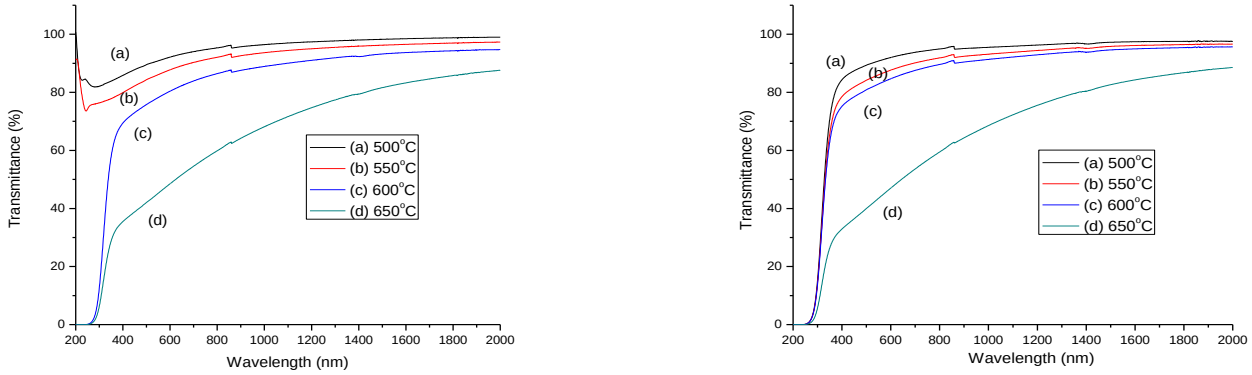

(a) (b)

Fig. 3. Transmittance spectrum for (a) pure a-C (b) a-C:N

The absorption coefficient (α) was calculated by the optical transmittance spectra of the film and the film thickness data, which indicates the measurement on how far the light with a specific wavelength or energy can penetrate into the thin film before being absorbed by that film. The α of a-C thin films could be calculated by Lambert's Law using

$$\alpha = \frac{1}{t} \ln\left(\frac{1}{T}\right) \qquad (1)$$

where t is the thickness and T is the transmittance of the film. Fig. 4 shows the variation of the absorption coefficient as a function of photon energy. Absorption coefficient at low energy is higher compared to the high energy, and further discussion on this phenomena can be related to the π-π* transition. Inside a-C, there are localized π electrons and the bonds between the π electron is inconsistent with any other allotrope of carbon. On the other hand, a-C contains high concentration of dangling bonds, which will affect the band gap value. Thus, since the localized π electrons play an important role in determining the optical properties of a-C, due to the reduced spatial overlapping of π and σ states wave overlapping, the contribution of σ-π* and π-σ* can be neglected [25, 26]. The optical band gap of pure a-C and a-C:N thin film was deduced using the Tauc plot [27] as shown in Figs. 5(a) and (b) in the absorption region (α~10^5-10^6 cm-1). The similar α value had also been reported for a-C deposited by surface wave microwave plasma CVD (~10^2-10^5 cm^{-1}) [28, 29], ion beam sputtering (~10^4-10^5 cm^{-1}) [30].

* Corresponding author. Tel.: +603-55441883
E-mail address: nurfadzilahahmad@yahoo.com

Available online at www.sciencedirect.com

SciVerse ScienceDirect

Procedia Engineering 00 (2012) 000–000

Procedia Engineering

www.elsevier.com/locate/procedia

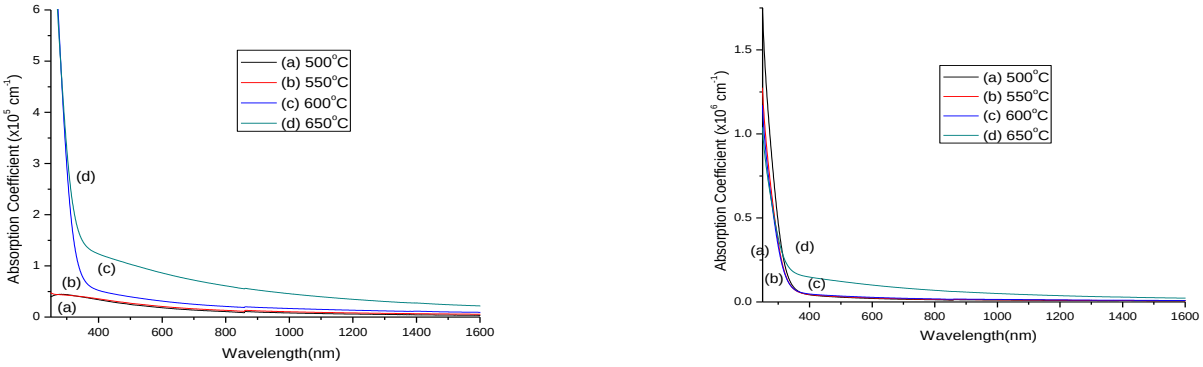

(a) (b)

Fig. 4. Absorption coefficient spectra for (a) pure a-C (b) a-C:N

The optical band gaps (E_g) for amorphous semiconductors were obtained by Tauc relationship $(\alpha h\nu)^{1/2} = B(E_g - h\nu)$, where α is the absorption coefficient, B is the Tauc parameter and $h\nu$ is the photon energy. The intercept of the Tauc's slope in the photon energy axis gives the optical gap, E_g. Highest band gap was noted at 500°C, 0.9 eV for undoped and 0.75 eV for N doped and the E_g decrease as temperature increase. The higher optical band gap at lower temperature is believed due to the increase in dangling bonds that leads to higher spin density and justifying the decrease in the grain size [31].

On the other hand, the decrease in E_g when doping is intoduced can be speculated that the N incorporation induced graphitization due to increase of sp^2 and this is also responsible for reduction in I_D/I_G ratio in Raman measurement [5]. Thus, the narrow optical band gap investigated from the N incorporation is evidently results from the increase in π/π^* electronic states on the sp^2 graphitize sites. From the E_g results, it is noted that there is a small gap between the valence and conduction band that the thermal or other excitations can bridge the gap. The interaction between the lattice phonons and the free electrons and holes will also affect the band gap to a smaller extended.

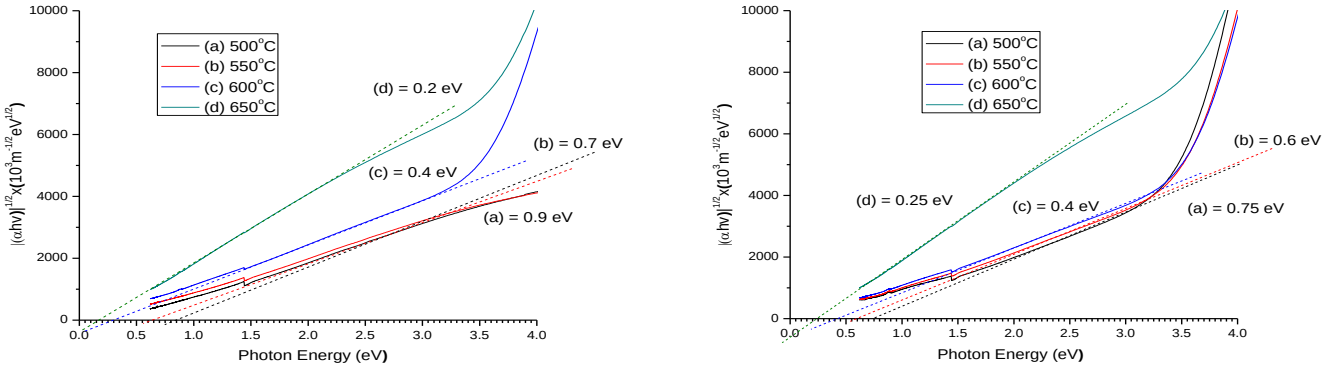

(a) (b)

Fig. 5. Tauc plot for (a) pure a-C (b) a-C:N

4. Conclusions

Pure amorphous carbon (a-C) and nitrogen doped amorphous carbon (a-C: N) thin films were prepared using Thermal Chemical Vapor Deposition (CVD) with deposition temperature ranging from 500°C to 650°C using camphor ($C_{10}H_{16}O$) as a precursor from natural source. The structural properties of amorphous carbon (a-C) thin films with Nitrogen Incorporation from Natural Source has been investigated using standard measurement techniques and the Raman analyses due to nitrogen

* Corresponding author. Tel.: +603-55441883
E-mail address: nurfadzilahahmad@yahoo.com

incorporation are discussed. For both undoped and nitrogen doped samples, two asymmetric peaks at around 1350 cm^{-1} (D-peak) and 1590 cm^{-1} (G-peak) were obtained for both cases which are typical for a-C. G-peak shifts to higher wave number from 1568 to 1592 cm^{-1} and becomes narrower as the temperature increases (FWHM decrease) indicates the increase of crystallinity and graphitization in the C-C phase. The D-peak however becomes wider as temperature increase (FWHM increase). The difference in intensity value from pure a-C and nitrogen doped a-C is due to the increasing sp^2 phase when doping is introduced. Optical measurement results in high transmittance for sample at 500^oC and 550^oC, with high absorption coefficient value, ~10^5 - 10^6 cm^{-1}. However, a-C: N has slightly higher transmittance compared to pure a-C. The high transmittance could be explained to be related to the reduction of the sp^2 phase in the film, which absorbs the visible wavelength range. Further, the narrow optical band gap investigated from the N incorporation is evidently results from the increase in π/π^* electronic states on the sp^2 graphitize sites.

Acknowledgment

The authors would like to thank the Research Management Institute (RMI), Universiti Teknologi MARA (UiTM); and Ministry of Higher Education (MOHE); Malaysian Government for the financial support.

References

[1] C. W. Chen and J. Robertson, 2006. Surface atomic properties of tetrahedral amorphous carbon, Diamond and Related Materials, vol. 15, pp. 936.
[2] V. Rigato, G. Maggioni, D. Boscarino, G. Mariotto, E. Bontempi, A. H. S. Jones, D. Camino, D. Teer, and C. Santini, 1999. Ion beam analysis and Raman characterisation of coatings deposited by cosputtering carbon and chromium in a closed field unbalanced magnetron sputter ion plating system, Surface and Coatings Technology, vol. 116- 119, pp. 580.
[3] Y. S. Park and B. Hong, 2008. Characteristics of sputtered amorphous carbon films prepared by a closed-field unbalanced magnetron sputtering method, Journal of Non-Crystalline Solids, vol. 354, pp. 5504.
[4] J. Podder, M. Rusop, T. Soga, and T. Jimbo, 2005. Boron doped amorphous carbon thin films grown by r.f. PECVD under different partial pressure, Diamond and Related Materials, vol. 14, pp. 1799.
[5] S. M. Mominuzzaman, M. Rusop, T. Soga, T. Jimbo, and M. Umeno, 2006. Nitrogen doping in camphoric carbon films and its application to photovoltaic cell, Solar Energy Materials and Solar Cells, vol. 90, pp. 3238.
[6] K. Abe and O. Eryu, 2006. Optical properties of amorphous carbon films implanted with nitrogen, Nuclear Instruments and Methods in Physics Research Section B: Beam Interactions with Materials and Atoms, vol. 242, pp. 637.
[7] J. Besold, R. Thielsch, N. Matz, C. Frenzel, R. Born, and A. MÃbius, 1997. Surface and bulk properties of electron beam evaporated carbon films, Thin Solid Films, vol. 293, pp. 96.
[8] A. Zeng, Y. Yin, M. Bilek, and D. McKenzie, 2005. Ohmic contact to nitrogen doped amorphous carbon films," Surface and Coatings Technology, vol. 198, pp. 202.
[9] S. Liu, G. Wang, and Z. Wang, 2007. Study of the conductivity of nitrogen doped tetrahedral amorphous carbon films," Journal of Non-Crystalline Solids, vol. 353, pp. 2796.
[10] Diane S. Knight and William B. White, 1989. Characterization of diamond films by Raman spectroscopy, Journal of Materials Research, vol. 4 , pp 385.
[11] T.-L. Sung, Y.-A. Chao, C.-M. Liu, K. Teii, S. Teii, and C.-Y. Hsu, 2011. Deposition of amorphous hydrogenated carbon films on Si and PMMA by pulsed direct-current plasma CVD, Thin Solid Films, vol. 519, pp. 6688.
[12] S. Adhikari, D. C. Ghimire, H. R. Aryal, S. Adhikary, H. Uchida, and M. Umeno, 2006. Boron-doped hydrogenated amorphous carbon films grown by surface-wave mode microwave plasma chemical vapor deposition, Diamond and Related Materials, vol. 15, pp. 1909.
[13] X. R. Deng, Y. X. Leng, X. Dong, H. Sun, and N. Huang, 2011. Effect of hydrogen flow on the properties of hydrogenated amorphous carbon films fabricated by electron cyclotron resonance plasma enhanced chemical vapor deposition, Surface and Coatings Technology, vol. 206, pp. 1007.
[14] H. Liang, L. Delian, C. Xian, Y. Li, and Z. Yuqing, 2011. The deposition of a thick tetrahedral amorphous carbon film by argon ion bombardment, Applied Surface Science.
[15] A. M. M. Omer, S. Adhikari, S. Adhikary, M. Rusop, H. Uchida, M. Umeno, and T. Soga, 2006. Iodine doping in amorphous carbon thin-films for optoelectronic devices, Physica B: Condensed Matter, vol. 376, pp. 316.
[16] S. Prawer, K. W. Nugent, Y. Lifshitz, G. D. Lempert, E. Grossman, J. Kulik, I. Avigal, and R. Kalish, 1996. Systematic variation of the Raman spectra of DLC films as a function of sp2:sp3 composition, Diamond and Related Materials, vol. 5, pp. 433.
[17] S. A. Mohd Zobir, S. Abu Bakar, S. Abdullah, Z. Zainal, S. H. Sarijo, and M. Rusop, 2012. Raman Spectroscopic Study of Carbon Nanotubes Prepared Using Fe/ZnO-Palm Olein-Chemical Vapour Deposition, Journal of Nanomaterials, vol. 2012.
[18] S. Kamikura, T. Uchida, K. Naka, T. Asaji, H. Uchiyama, and Y. Yoshida, 2011. Single-walled carbon nanotube

* Corresponding author. Tel.: +603-55441883
E-mail address: nurfadzilahahmad@yahoo.com

growth using cobalt nanoparticles prepared by vacuum deposition on a surface-active liquid, Diamond and Related Materials, vol. 20, pp. 863.
[19] S. M. Mominuzzaman, K. M. Krishna, T. Soga, T. Jimbo, and M. Umeno, 2000. Raman spectra of ion beam sputtered amorphous carbon thin films deposited from camphoric carbon, Carbon, vol. 38, pp. 127.
[20] M. Rusop, T. Soga, T. Jimbo, 2005. Investigation of structural properties of amorphous carbon nitride thin films prepared by xenon cloride pulsed laser deposition of camphoric carbon precursor, Journal of Material Science, vol. 16, pp. 367.
[21] M. Rusop, A. Omer, S. Adhikari, S. Adhikary, H. Uchida, T. Soga, T. Jimbo, and M. Umeno, 2006. Effects of annealing temperature on the optical, bonding, structural and electrical properties of nitrogenated amorphous carbon thin films grown by surface wave microwave plasma chemical vapor deposition, Journal of Materials Science, vol. 41, pp. 537.
[22] D. Beeman, J. Silverman, R. Lynds, and M. R. Anderson, 1984. Modeling studies of amorphous carbon, Physical Review B, vol. 30, pp. 870.
[23] Suriani Abu Bakar, Salina Muhamad, and Puteri Sarah Mohamad Saad, 2011. Effect of temperature on the growth of vertically aligned carbon nanotubes from palm oil, Defect and Diffusion Forums, vol. 312, pp. 900.
[24] K. Chakrabarti, R. Chakrabarti, K. K. Chattopadhyay, S. Chaudhuri, and A. K. Pal, 1998. Nano-diamond films produced from CVD of camphor, Diamond and Related Materials, vol. 7, pp. 845.
[25] R. Gharbi, M. Fathallah, N. Alzaied, E. Tresso, and A. Tagliaferro, 2008. Hydrogen and nitrogen effects on optical and structural properties of amorphous carbon, Materials Science and Engineering: C, vol. 28, pp. 795.
[26] G. Fanchini, S. C. Ray, and A. Tagliaferro, 2003. Density of electronic states in amorphous carbons," Diamond and Related Materials, vol. 12, pp. 891.
[27] T. J, 1968. Optical properties and electronic structure of amorphous Ge and Si, Materials Research Bulletin, vol. 3, pp. 37.
[28] M. Rusop, S. Adhikari, A. M. M. Omer, T. Soga, T. Jimbo, and M. Umeno, 2006. Effects of methane gas flow rate on the optoelectrical properties of nitrogenated carbon thin films grown by surface wave microwave plasma chemical vapor deposition, Diamond and Related Materials, vol. 15, pp. 371.
[29] S. Adhikari, S. Adhikary, A. M. M. Omer, M. Rusop, H. Uchida, T. Soga, and M. Umeno, 2006. Optical and structural properties of amorphous carbon thin films deposited by microwave surface-wave plasma CVD, Diamond and Related Materials, vol. 15, pp. 188.
[30] K. M. Krishna, Y. Nukaya, T. Soga, T. Jimbo, and M. Umeno, 2001. Solar cells based on carbon thin films, Solar Energy Materials and Solar Cells, vol. 65, pp. 163.
[31] J. Podder, M. Rusop, T. Soga, and T. Jimbo, 2005. Boron doped amorphous carbon thin films grown by r.f. PECVD under different partial pressure, Diamond and Related Materials, vol. 14, pp. 1799.

* Corresponding author. Tel.: +603-55441883
E-mail address: nurfadzilahahmad@yahoo.com

Available online at www.sciencedirect.com

SciVerse ScienceDirect

Procedia Engineering 00 (2012) 000–000

Procedia Engineering

www.elsevier.com/locate/procedia

5th BSME International Conference on Thermal Engineering

Photoluminescence Characteristics of Silicon Quantum Dots Nanoparticles (SQDNs) Embedded on Glass Surface

C.H Rosmani [a],S. Abdullah[b] , and M. Rusop[c]

NANO-Sci TECH Centre,Institute of Science
Faculty of Applied Science;
NANO-ElecTronic Centre, Faculty of Electrical Engineering
Universiti Teknology MARA (UiTM),40450 Shah Alam,Selangor,Malaysia

Abstract

Photoluminescence of silicon quantum dots nanoparticles (SQDNs) embedded on glass surface was measured by using Photoluminescence Spectroscopy (PL) at room temperature with a laser source of 512.32 nm. SQDNs were prepared by using electrochemical etching process, used p-type silicon (Si) wafer. The Si wafer was etched at constant time using a current density 20 $mAcm^{-2}$ for 20 min and continuously with 30 min until the wafer surface became flakes. These flakes were grinded to be SQDNs and thus produced were embedded on glass surface, by using different ratio of dionize water (DI) and hydrofluoric acid (HF). This different ratio of DI:HF will be defect the glass surface. Photoluminescence result showed the higher when SQDNs were embedded on glass surface with DI:HF 1:5, the second higher was 1:8 ant the less was 1:2. In this paper, size for SQDNs were constant with size 1.4 nm by using Sherrer equation from X-ray Diffaraction (XRD) result.

Keywords: SQDN; Silicon Quantum Dots Nanoparticles; Porous Silicon; PSi; Electrochemical; Photoluminescence.

1. Introduction

The increasing in using silicon quantum dots nanoparticle (SQDNs) embedded in silicon (Si) as light sources for many application such as solar cells, light emitting diode (LED) and optoelectronic device [1-3]. Semiconductor nanocrystals (NC) ,the so called quantum dots (QD) are potential building blocks of future nanoelectronic and nanophotonics [4-6]. Si based light sources would permit devices containing both optical and electrical components. The nanosize semiconductor materials consists band gap that strongly dependent on cluster size or layer thickness. SQDNs used to produce light of greater intensity over a wider wavelength range than devices fabricated from bulk silicon [7, 8].

SQDNs is formed from porous silicon (PSi) by using electrochemical method and become SQDNs when their size become smaller [3]. PSi is a form of the chemical element Silicon (Si) which has an introduced nanoporous holes in its microstructures, rendering a large surface to volume ratio in the order of $500m^2/cm^2$ [9]. PSi was discovered by Uchir in studying the electro polishing of silicon surface using HF. PSi was obtained by using electrochemically etching a Si wafer was explored leading by Canham and co-worker [10]. PSi efficiently emits visible light at room temperature. PSi is well known, inexpensive integrable with Si technology and very sensitive to the environment due to its large surface versus volume ratio [11-13].

There are two main ways to synthesize Si nanoparticles, include top-down and bottom-up processes. The top down process is based on high energy dispersing of bulk material and bottom-up based on formation of nanoparticles which is form precursor molecules [14]. From previous studied, Si-based material was produced by silane gas decomposition, cosputtering, ion implantation technique , have efficiently demonstrated PL in the visible [7,13]. The majority of previous investigations have focused on SQDNs embedded in an oxide matrix, but unfortunately, these material provide fairly limited physical access to the interface structures ,which is can be controlled to a limited degree by thermal processing at elevated temperatures [7, 13, 15].

In this paper, the important objective is want to investigate the optical properties of SQDNs when embedded on the glass surface. The PL measurement was done in the room temperature with laser wavelength sources 512.32 nm. The images form scanning electron microscopy (SEM) was done to surface morphology and X-ray Diffraction (XRD) to know the size of SQDNs by using Sherrer equation

1.1 Quantum Dots

Quantum dots are semiconductor whose conducting characteristic closely related to the size and shape of the individual crystal. Generally, the smaller the size of the crystal, the larger the band gap. The greater the difference in energy between the highest valence band and the lowest conduction band [10]. Quantum dots also known as nanocrystals, are a special class of material known as semiconductor which are crystal composed of periodic group of II-IV, III-V or IV-VI materials. Quantum dots are unique class of semiconductor materials because they are so small, ranging from 2-10 nanometers in diameter . A quantum dost has a discrete quantized energy spectrum.

From this paper by using electrochemical process to prepare PSi [16]. The PL mechanism has been intensively discuss in different models proposed, recombination of quantum confined electron-hole pairs ,recombination in siloxenes , amorphous of Si, surface state related to silicon-oxygen or hydrogen bond [4]. From the past decade, interest in nanoparticles strongly increasing. Form previous studied, many researchers have found the luminescence peak position of SQDNs can be tuned by controlling the size of SQDNs [17]. As the size of particles become smaller, the surface area per unit volume substantially increases ,thus dramatically changing the particle properties. This may result in unique added value to the particulate materials because of their specific chemical, electro-magnetic. Optical or other physical properties [18].

Quantum dots might be used as frequency converters to better match the spectrum of the incoming radiation to the spectral efficiency [8]. The term quantum dots describes a nanocrystal (NC) that is small enough (few nm) that it confines the wave function of the excited electron. In principle, the fluorescence spectroscopic data also provide information on the band gap in the small particles and are therefore related to the particle size if quantum confinement is the mechanism for generating emission at energies higher than bulk band gap [16].

Quantum dots also called nanoclusters or nanocrystals, are a perfect example of the quantum mechanical particle in a box where the energy of a particle decrease as the size of the box (quantum dot) increases [19]. In quantum structures, the spatial confinement of the carries will spread the wave function and thus increase the probability for a direct no-phonon optical transition [20]. The PL mechanism has been intensively debated in many different models proposed recombination of quantum confined electron–hole pairs, recombination in siloxenes, amorphous phase of Si, surface states related to silicon-oxygen or hydrogen bonds [21]. Some experiments demonstrated a technique for fabricating a Si quantum well (QW) with a confined energy level of 1.7 eV demonstrated by photoluminescence for a QW thickness of 1nm[11]. The luminescence efficiency due to the localization of electron-hole pairs, which would indicate the increased absorptivity also required for solar cell application [22].

2. Experimental

2.1 Preparation of the Free Standing Psi

Cleaning Si were first to clean and remove trace materials from the surface before the etching process. The wafer was cut to size of 2 cm x 2 cm by using diamond cutter. The Si wafer was washed by using DI and HF by using ultrasonic bath with temperature 35 ^{0} C at 10 min. After washed with DI and HF, the wafers were dried by using nitrogen gas blow and

keep in ambient temperature at 30 min for the preparation of the free standing PSi electrochemical etching process was used with Si wafer p-Si with <100> oriented [16].

The etching was prepared by anodization in chemicals of electronic HF electrolyte and ethanol with ratio 1:1. The sample was put in the Teflon under halogen lamp. The halogen lamp used for accelerates the chemical reaction for electrochemical etching process and the band gap of nanocrystal in the PL layer become larger than the incident photon energy of illumination light [23]. The etching process was at 30 min and the current density at 50 $mAcm^{-2}$. The halogen lamp is very important for p-types Si to PSi because holes are needed for the electrochemical etching process [23].

2.2 Preparation of SQDNs on the Glass Surface

The surface of PSi would be peel off and become flakes from substrates and known as free standing PSi. The flakes from free standing PSi would be grind mechanically. The parameter for grinding process was 450 rpm for 4 hour. The glass for embedding process was cut into size of 1 cm x1 cm by using diamond cutter. This glass was washed by using acetone and methanol in the ultrasonic bath at temperature 40 ^{0}C at 5 minutes. The preparation of the glass in DI;HF with different ratio of 1:2, 1:5 and 1:8. From previous papers were investigated, Si embedded in an oxide matrix by using drop by drop method [13], chemical vapor deposition [7], sol-gel dip coating method [8] and thermal annealing [24]. In this paper, embedding process of SQDNs in glass surface by immersing glass in DI:HF with different ratio of HF. For this process polytetrafluoroethylene (PTFE) beaker was used for avoid corrosive by HF solution. The DI : HF were 1:2, 1:5 and 1:8 immersing process was in 1 hour.

3. Result and Discussion

3.1 Characterization

The samples were checked by using photoluminescence spectroscopy (PL) for the optical properties, the surface morphology by using SEM and X-ray diffraction (XRD) for particle sizes. The PL characterize by using laser with wavelength 512.35 nm.

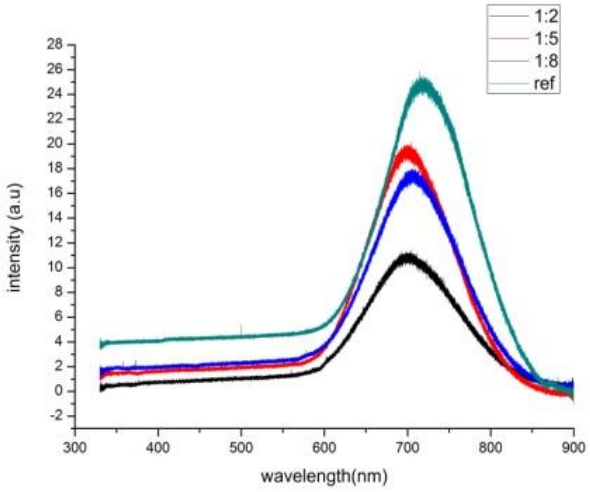

Fig. 1. PL measurement under room temperature with different ratio of DI:HF

From the Fig.1, the intensity of the optical properties for SQDNs was less when the ratio of DI:HF become higher. In this project, the size of SQDNs were constant. This is important to know the effect of defect on the glass surface even though used same size of SQDNs. The position of these PL band depend on Si crystalline sizes [6]. Fig.1 showed PL measurement at room temperature. In this research laser of wavelength 512.35 nm was used. During measurement, the range of scanning

was set between 300 nm to 900 nm, in general the emission are falls into the category of silicon band in blue-red region. The SQDNs related with luminescence that the increase in the dot size would reduce the emission energy [2].

Fig.1 has been showed the peaks in the range 300 nm to 900 nm on the PL spectra where the maximum is at 659 nm. Observing on room temperature PL spectra, SQDNs showed intense red light emission. The red-shift in the photoluminescence spectrum might suggest the contribution from the part of SQDNs is enhance [2]. The PL graph showed that the different peak and intensity when SQDNs embedded on the glass surface with different ratio of HF:DI. For the reference sample was not embedded in glass because used as reference for comparisons to the other samples. The second higher was for ratio 1:5, the third 1:8 and the lower was 1:2.

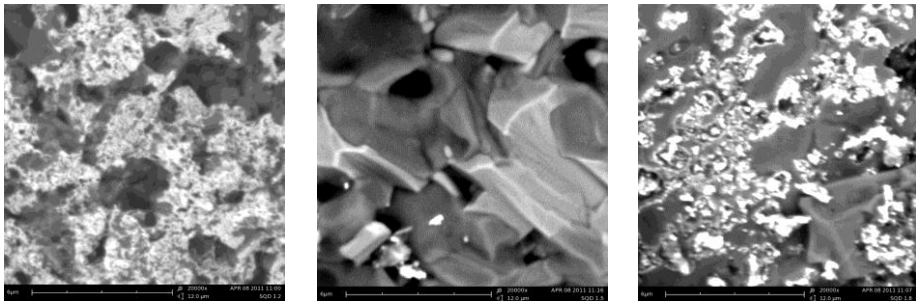

(a) (b) (c)

Fig. 2 SEM image for the SQDNs embedded in the glass with HF:DI (a) 1:2 (b) 1:5 (c) 1:5

From Fig.2 (a), (b), (c) above showed the defect of glass surface when immersed in different ratio of HF:DI. When more concentration HF was used ,more defect of the glass surface and thus more SQDNs were embedded on the glass surface. The magnification was used was 2000x. Scanning electron microscope (SEM) is a one type of electron microscope that can get the image by scanning the samples with high-energy beam of electron in a raster scan pattern. The interaction between the atoms and the surface make up the sample producing signals that's contains information about the sample's surface topography, composition and other properties .SEM is used for to know the structure and surface morphology of the particle.

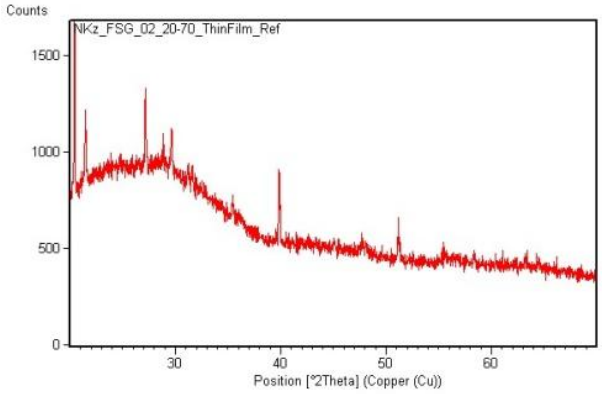

Fig.2 Graph XRD pattern for SQDNs without embedded on the glass surface

From XRD patterns, XRD was used to reveal information about the crystallographic structure ,chemical composition and physical properties of materials and thin films. The size of SQDNs was calculated by using Scherrer equation :

$$D = k \lambda / \beta \cos \theta , \qquad k= 0.9 \qquad (1)$$

λ = 0.15406 nm (wavelength for alpha)
β = full width half maximum

The XRD model is PAN analytical X'Pert PRO with maximum voltage 60kv and maximum current is 60 mA. This XRD for SQDNs was not embedded in glass because as reference for other SQDNs which was embedded on glass. The higher peak when range in 39 to 40 degree. The crystal system is orthorhombic. The size for SQDNs in this experiment was 1.4 nm by using Scherrer equation. In this project, the size of the SQDNs were constant, the main important in this paper to know the effect of optical properties of SQDNs when embedded in the glass.

4. Conclusion

In this paper, the concentration of HF has been effected on the glass surface. Thus the intensity of PL of SQDNs were changed. Even though the size of SQDNs were same but the intensity of photoluminescence was changed when SQDNs embedded on the glass surface. Thus it can be said that ,the optical properties of SQDNs were changed when embedded on the glass surface. When more defect the glass surface, the intensity of PL of SQDNs were decrease.

Acknowledgements

The work has been carried out under a project under Research Management Institute (RMI) University Teknologi MARA (UiTM) Malaysia.

References

[1] Hyldahl , M.G , S.T. BAILEY, and B.P.Wittermershaus, 2009. Photo –Stability and performance of CdSe/ZnS quantum dots in luminescent solar concentrators.Solar Energy 83(4),p.566-573
[2] Pei, Z. and H.L. Hwang,2003. Formation of silicon nano-dots in luminescent silicon nitride. Applied Surface Science. 212-213: p. 760-764..
[3] Jang, H,2003. Photoluminescence quenching of silicon nanoparticles in phospholipid vesicle bilayers. Journal of Photochemistry and Photobiology A: Chemistry. 158(2-3): p. 111-117.
[4] Juhasz, J.V.R. and J. Linnros,2002. Photoluminescence from single silicon quantum dots at room temperature. Journal of Luminescence. 98: p. 15-22.
[5] Kelly, M.T. and A.B. Bocarsty,1998. Mechanisms of photoluminescent quenching of oxidized porous silicon Applications to chemical sensing. Coordination Chemistry Reviews, 1998. 171: p. 251-25
[6] Rodriguez, A., J. Arenas, and J.C. Alonso, 2012.Photoluminescence mechanisms in silicon quantum dots embedded in nanometric chlorinate silicon nitride films. Journal of Luminescence, 2012. 132(9): p. 2385-2389.
[7] Schüler,2007. Quantum dot containing nanocomposite thin films for photoluminescent solar concentrators. Solar Energy. 81(9): p. 1159-1165.
[8] Choi, B.-J,.2007. Preparation of silicon nanoparticles for device of photoluminescence. Surface and Coatings Technology, 2007. 201(9-11): p. 5003-5006.
[9] L.Kovtyukhova, N.2000. Surface Sol-Gel Synthesis of Ultrathin Semiconductor Films. Chem.Mater. 12: p. 383-389.
[10] Jane, A.,Dronov.R,Hodges et al.2009, Porous silicon biosensors on the advance. Trends Biotechnol. 27(4): p. 230-9.
[11] Li, P.L., C. Gau, and C.W. Liu,2012. Correlation between photo response and nanostructures of silicon quantum dots in annealed Si-rich nitride films. Thin Solid Films, 2012.
[12] Lockwood.R,McFarlane.S,Rodriguez Nunez, et al,2011. Photoactivation of silicon quantum dots. Journal of Luminescence. 131(7): p. 1530-1535.
[13] Kravitz, Keren,Kamyshny, et al.2010. Solid state synthesis of water-dispersible silicon nanoparticles from silica nanoparticles. Journal of Solid State Chemistry. 183(6): p. 1442-1447.
[14] Liuy, Xi,Wu,Xiaoming, et al. 2012, Quantum dots photoluminescence based thin film thermal conductivity metrology. Sensors and Actuators A: Physical,.
[15] Lie, L.H.Mark Duerdin,Eimer M.Tuite et al.2002. Preparation and characterisation of luminescent alkylated-silicon quantum dots. Journal of Electroanalytical Chemistry. 538-539: p. 183-190
[16] Jiang, L., X. Zeng, and X. Zhang,2011. The effects of annealing temperature on photoluminescence of silicon nanoparticles embedded in SiNx matrix. Journal of Non-Crystalline Solids. 357(10): p. 2187-2191
[17] Van Ommen, J.Ruud,Yurteri,Caner.U, et al.2010, Scalable gas-phase processes to create nanostructured particles. Particuology. 8(6): p. 572-577.
[18] Trivedi, E.R. and S.L. Hatch, Synthesis and Size Dependent Properties of CdSe Quantum Dots. Department of Chemistry. IL 60208.
[19] Larsson, M.Elfving,A.Holtz, et al.2003, Photoluminescence study of Si/Ge quantum dots. Surface Science. 532-535: p. 832-836.
[20] Valenta, J., R. Juhasz, and J. Linnros,2002. Photoluminescence from single silicon quantum dots at room temperature. Journal of Luminescence, 2002. 98: p. 15-22
[21] Conibeer, Gavin Green,Martin Cho et al.2008. Silicon quantum dot nanostructures for tandem photovoltaic cells. Thin Solid Films. 516(20): p. 6748- 6756
[22] Kanemitsu, Y. and S. okamoto,1997. Visible luminescence from silicon quantum dots and wells. Materials Science and Engineering. B48: p. 108-115
[23] Kim, B.H., R.F. Davis, and S.-J. Park,2012.Optical property of silicon quantum dots embedded in silicon nitride by thermal annealing. Thin Solid Films. 518(6): p. 1744-1746

Available online at www.sciencedirect.com

SciVerse ScienceDirect

Procedia Engineering 00 (2012) 000–000

Procedia Engineering

www.elsevier.com/locate/procedia

5th BSME International Conference on Thermal Engineering

Atomic Force Microscopy Characterization of Latex Nanoparticles Synthesized by Slow Drying Process of Nano-Emulsion Polymerization

N.F. Hassmoro[a,b,*], S. Abdullah[a,b], and M. Rusop[a,c]

[a]*NANO-SciTech Centre, Institute of Sciences;*
[b]*Faculty of Applied Sciences;*
[c]*NANO-ElecTronic Centre, Faculty of Electrical Engineering;*
Universiti Teknologi MARA (UiTM), 40450 Shah Alam, Selangor, Malaysia

Abstract

The nano-emulsion polymerization method was used to synthesize the latex nanoparticles. Two set of samples are prepared by fast drying and slow drying process. For each process they have a two different amount of monomer. The monomer consists of butyl methacrylate (BMA), butyl acrylate (BA), and methacrylic acid (MAA). The average particle size of latex by fast drying process is 31.94 nm for low amount of monomer and 19.59 nm for high amount of monomer. By slow drying process the average particle size of latex nanoparticles for low and high amount of monomer are 26 nm and 8.62 nm respectively. All the samples that were prepared are characterized by Atomic Force Microscopy (AFM). We have found that the butyl methacrylate (BMA) content in between 6 g and 10 g has sensitively effect to the synthesization of nano-polymer for the both method of fast drying process and slow drying process of nano-emulsion polymerization method.

Keywords: Latex nanoparticles; Emulsion polymerization; Drying process; Atomic Force Microscopy; AFM

1. Introduction

Polymer nanoparticles with smaller size distribution have a wide range of applications such as paints, coatings, and adhesives [1-4]. Emulsion polymerization is the common technique for the production of colloidal polymer suspensions (latex) where the polymer is finely distributed in a liquid dispersion medium in the form of stable individual particles [5]. The basic ingredients required for an emulsion polymerization are the monomer, the dispersion medium, the emulsifier, and the initiator. An emulsion of monomer droplets is formed in the continuous dispersion medium when all the ingredients are mixed together within a certain temperature range. Initiator cause the formation of radical mechanism then propagates the polymerization. A stable emulsion of polymer will be formed when the polymerization is completed [6-8].

Based on the numerous reports of the film formation of latex, it is widely accepted that there are three main stages during drying process of the latex film [9-11]. First stage, water will evaporates from the stable dispersion that was applied onto a substrate, and the polymer particles become proximity. The evaporation rate of water decreases when enter to the next stages and deformation of the particles occurs due to capillary pressure. Lastly, polymer diffusion occurs across the boundary and forms a homogeneous film.

* Corresponding author. Tel.: +60-13-714-8271.
E-mail address: nurfarahinhassmoro@gmail.com

In this work, the latex nanoparticles solution at different amount of monomer is prepared via nano-emulsion polymerization method. The samples have been characterized by Atomic Force Microscopy (AFM) to study the effect of particle size using different drying process.

2. Experimental

2.1. Materials

The monomer content of butyl methacrylate (BMA), butyl acrylate (BA), and methacrylic acid (MAA), N,N,N',N'-tetramethylethylenediamine (TMEDA) (accelerator for initiator), 2-amino-2-methyl-1-propanol (AMP), and ethanol were purchased from Merck without further purification. Ammonium persulfate (APS) (polymerization initiator), sodium dodecyl sulfate (SDS), and ammonia solution 25 % brought from R&M chemical were used as received. Deionized water was used throughout the experimental work.

2.2. Polymerization

A typical polymerization procedure has been discussed elsewhere [4,7,12,13] but here we are proposed a simplest method where all of the chemical used are mixed together in a beaker without bubbling nitrogen gas. First, four type of solutions are prepared, monomer solution that consist of BMA (5.7 g and 9.7 g), 2.1 g of BA, and 0.2 g of MAA. Then acceletor solutions consist of 0.046 g of TMEDA and 5 g of de-ionized water. Initiator solution consist of 0.1 g APS and 5 g of de-ionized water and lastly AMP solution that consist of 5 g 2-amino-2-methyl-1-propanol (AMP) and 5 g of de-ionized water.

Next 0.3 g monomer solution, 1.0 g of SDS, 0.1 g of ethanol, and 78.7 g of de-ionized water was poured into a beaker. The pH is adjusted to 9.0 - 10.0 by using ammonia. The nano-emulsion is heated to 40 ^{o}C and stirred about 600 revolutions per minute (rpm). Next acceletor solution and initiator solution were added into the nano-emulsion with continue stirring and maintain temperature. 0.1 g of ethanol was added to the rest of monomer solution and later was added drop-wise into the nano-emulsion. After addition was completed, stirring continue at 40 ^{o}C for about 2 - 3 h. The solution then cools to ambient temperature. AMP solution was slowly added to bring the pH to 9.2 - 9.5. The product is nearly transparent dispersion of polymer nanoparticles.

2.3 Drying Process

Glass substrate (2 cm x 2 cm) is cleaned to get a good adhesion of coating. The substrates were cleaned using acetone twice, methanol twice, and distilled water in ultrasonic bath for 5 minutes each. Finally, the substrates were blow with nitrogen gas. The cleaned glass substrates were dipped into the latex solution to obtain the thin film of latex nanoparticles. The sample were left at room temperature and going through different drying process. For fast drying process, sample was placed in a beaker and exposed in the air. For slow drying process, sample was placed in a beaker with aluminum foil wrapped on top of the beaker and small holes were made on the aluminum foil. This method is different from the previous study [11,14] as they used annealing process at high temperature.

2.2 Atomic Force Microscopy (AFM)

AFM XE-100 Park System was used to characterize all of the samples. It offers the visualization in three dimensional and gives the information of physical properties including size, morphology, surface texture, and roughness. It is able to provide high-resolution images of the film surfaces without any pre-treatment of sample under ambient condition. The scan rate was kept below 2 Hz to ensure adequate tracking of surface features. All images were auto-flattened by a computer to correct for drift in piezo extension over the time of the scan [15].

3. Results and discussion

The particle morphology of the latex nanoparticles are characterized and presented by the Atomic Force Microscopy (AFM) as showed in Fig. 1 and Fig. 2 for two different amount of butyl methacrylate (BMA). For each samples five point of the particle size has been taken to get the average size of the particle. The samples of Fig. 1a and Fig. 1b are prepared using a fast drying process. At 5.7 g of BMA, the particle sizes of the sample are 29.77, 30.65, 32.19, 33.27, and 33.82 nm (as point in Fig. 1a). The average of particle size is 31.94 nm and the agglomerate size is 3427 nm. For 9.7 g of BMA the

particle sizes are 18.42, 19.03, 19.57, 20.01, and 20.92 nm (as point in Fig. 1b). The average size of the particle is 19.59 nm and the agglomerate size 3770 nm. Fig. 2a and Fig. 2b display the results of slow drying process; at low amount of BMA the sizes of the particle are 24.44, 25.13, 26.02, 26.72, and 27.69 nm (as point in Fig. 2a). The average size of particle is 26 nm and the agglomerate size is 565 nm. For higher amount of BMA the sizes of the particle are 7.32, 7.65, 8.05, 9.97, and 10.11 nm (as point in Fig. 2b). The average size and the agglomerate size of the particle are 8.62 nm and 907 nm respectively. The particle size of the samples was measured from peak-to-valley distances while the agglomerate size of the samples is based on the peak-to-peak distances. The roughness surface for Fig. 1a, 1b, 2a, and 2b is found to be a slightly different where it is 5.357 nm, 3.726 nm, 5 nm, and 1 nm respectively. Table 1 gives the summarized of the AFM results.

Based on this results as the monomer increased the average particles of size will be decreased, it is contradict with the previous study [7,14] but agree with the theory where the higher the surfactant/monomer weight ratio, the smaller the particle size [16]. As previous study using annealing process at high temperature (90 ^{o}C) it was found to give a size of particle in the range of 29 nm [14]. From my humble knowledge, there are nobody reported the average particle of size below 8.62 nm. By using the slow drying process it is successful to give a narrower average particle sizes. The agglomerate size become bigger as the BMA amount was added more. Slow drying process give the smaller average particles size compared with fast drying process.

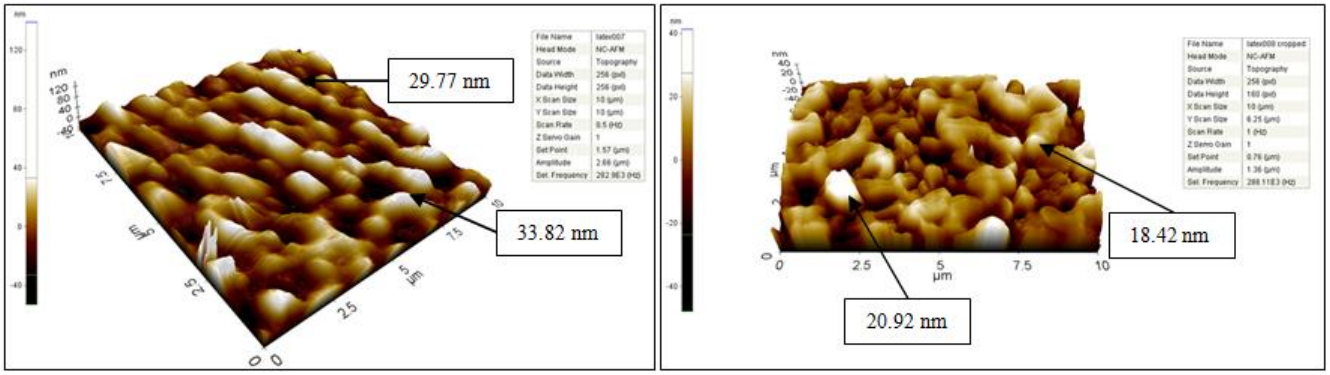

(a) (b)

Fig. 1. AFM image of latex using fast drying process: (a) 5.7 (b) 9.7 g of BMA

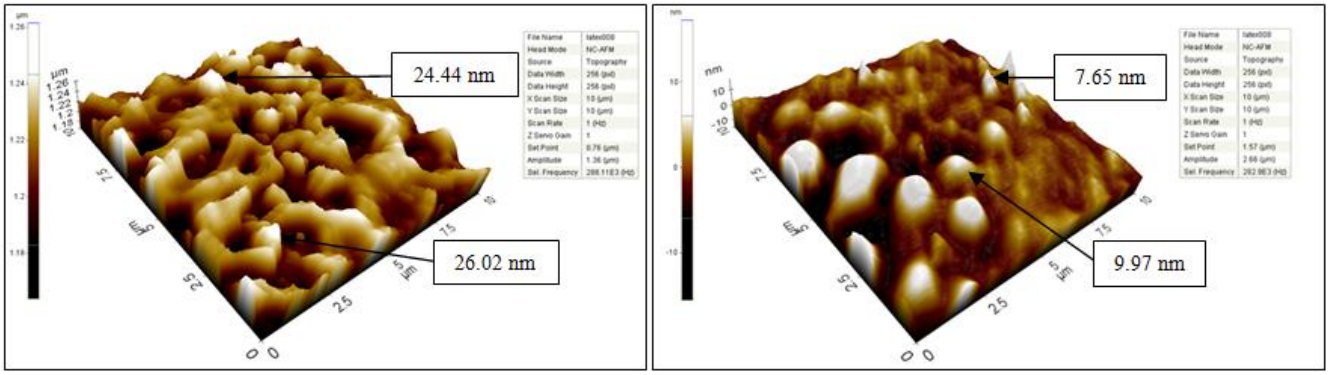

(a) (b)

Fig. 2. AFM image of latex using slow drying process: (a) 5.7 (b) 9.7 g of BMA

Table 1. Summarize of the results

Drying Process	BMA (*g*)	Size of particles (*nm*)	Average size of particles (*nm*)	Size of agglomerate particles (*nm*)	Roughness (*nm*)
Fast	5.7	29.77	31.94	3427	5.357
		30.65			
		32.19			
		33.27			
		33.82			
	9.7	18.42	19.59	3770	3.726
		19.03			
		19.57			
		20.01			
		20.92			
Slow	5.7	24.44	26.00	565	5.000
		25.13			
		26.02			
		26.72			
		27.69			
	9.7	7.32	8.62	907	1.000
		7.65			
		8.05			
		9.97			
		10.11			

3.1 Conclusion

In summary, we prepared the latex nanoparticles via the nano-emulsion polymerization method. The drying process is optimized in order to get small average particle size of latex. High amount of monomer gives a better result compared to the low amount of monomer. Slow drying process of nano-emulsion polymerization method is found to give a small average size of nano-particle that contribute to the large surface area as has been confirmed by Atomic Force Microscopy (AFM) characterization. On results have shown that, the roughness surfaces of morphology are slightly to be different for all samples prepared at different amount of butyl methacrylate (BMA). The average particle size of latex by fast drying process is 31.94 nm for low amount of monomer and 19.59 nm for high amount of monomer. By slow drying process the average particle size of latex nanoparticles for low and high amount of monomer are 26 nm and 8.62 nm respectively. Therefore, we have found that the butyl methacrylate (BMA) content in between 6 g and 10 g has sensitively effect to the synthesization of nano-polymer for the both method of fast drying process and slow drying process of nano-emulsion polymerization method.

Acknowledgements

Authors are gratefully acknowledged for the financial support to the MyBrain15 Sponsorship Programme, Malaysian Government and also to the Research Management Institute, Universiti Teknologi MARA (UiTM), Shah Alam, Selangor, Malaysia.

References

[1] Yu Xing Peng, Zhao Hui Zheng, Xiao Bin Ding, Wen Chuan Zhang, Zhong Hu Ye, 2003. Nanometer Polymer Latex Dispersion and its Application in Water-based Coating, Progress in Organic Coatings 48, pp. 161-163.

[2] Xiang Z. Kong, Xiaoli Zhu, Xubao Jiang, Xiufen Li, 2009. Preparation and Full Characterization of Cationic Latex of Styrene-butyl Acrylate, Polymer 50, pp. 4220-4227.
[3] Xuefeng Hu, Jieyu Zhang, Wantai Yang, 2009. Preparation of Transparent Polystyrene Nano-latexes by an UV-induced Routine Emulsion Polymerization, Polymer 50, pp. 141-147.
[4] Xiuxia Wang, Guoqiao Lai, Zhigang Jiang, Yifeng Zhang, 2006. Synthesis of Water-soluble Hyperbranched Polymer and its Application in Acrylic Latex, European Polymer Journal 42, pp. 286-291.
[5] Klaus Tauer, Hugo Hernandez, Steffen Kozempel, Olga Lazareva, Pantea Nazaran, 2008. Towards a Consistent Mechanism of Emulsion Polymerization – New Experimental Details, Colloid Polym Sci 286, pp. 499-515.
[6] Graham Cooper, Franz Grieser, Simon Biggs, 1996. Butyl Acrylate/Vinyl Acetate Copolymer Latex Synthesis Using Ultrasound As an Initiator, Journal of Colloid and Interface Science 184, pp. 55-63.
[7] Harald Wutzel, Wolfgang M. Samhaber, 2007. Exploring the Limits of Emulsion Polymerization of Styrene for the Synthesis of Polymer Nanoparticles, Monatshefte Fur Chemie 138, pp. 357-361.
[8] Kalin I. Dragnevski, Athene M. Donald, 2008. An Environmental Scanning Electron Microscopy Examination of the Film Formation Mechanism of Novel Acrylic Latex, Colloids and Surfaces A: Physicochem. Eng. Aspects 317, pp. 551-556.
[9] Alexander F. Routh, William B. Russel, 2001. Deformation Mechanisms during Latex Film Formation: Experimental Evidence, Ind. Eng. Chem. Res. 40, pp. 4302-4308.
[10] Attila Olah, Mark A. Hempenius, Shan Zou, G. Julius Vancso, 2006. Adhesion Studies of Latex Film Surfaces on the Meso- and Nanoscale, Applied Surface Science 252, pp. 3714-3728.
[11] Petri Ihalainen, Kal Backfolk, Petri Sirvio, Jouko Peltonen, 2010. Topographical, Chemical, Thermal and Electrostatic Properties of Latex Film, Colloids and Surfaces A: Physicochem. Eng. Aspects 354, pp. 320-330.
[12] R. Seda Tigh, Vural Evren, 2005. Synthesis and Characterization of Pure Poly(acrylate Latexes, Progress in Organic Coatings 52, pp.144-150.
[13] Guangfeng Liu, Peng Liu, 2010. Synthesis of Monodispersed Crosslinked Nanoparticles Decorated with Surface Carboxyl Group via Soapless Emulsion Polymerization, Colloids and Surfaces A: Physicochem. Eng. Aspects 354, pp. 377-381.
[14] Xiao-zhong Qu, Yi Shi, Liu-sheng Chen, Xi-gao Jin, 2002. Effect of Particle Size on the Filming Process of Polystyene Latex Studied by AFM, Chinese Journal of polymer Science Vol. 20, no. 6, pp. 509-515.
[15] Abhijit A. Patel, Jianrong Feng, Mitchell A. Winnik, G. Julius Vancso, 1996. Characterization of Latex Blend Films by Atomic Force Microscopy, Polymer Vol. 37 No. 25, pp. 5577-5582.
[16] Abdelhamid Elaissari, 2003. Colloidal Polymer Synthesis and Characterization, Marcel Dekker Inc, New York. Basel, p.149

Available online at www.sciencedirect.com

SciVerse ScienceDirect

Procedia Engineering 00 (2012) 000–000

Procedia Engineering

www.elsevier.com/locate/procedia

5th BSME International Conference on Thermal Engineering

Enhanced Dielectric Properties of Tantalum Oxide Doped Barium Titanate Based Ceramic Materials

Rubayyat Mahbub[a], Takian Fakhrul[b], Md. Fakhrul Islam[c]*

[a,b]*Department of Materials and Metallurgical Engineering, Bangladesh University of Engineering and Technology, Dhaka-1000, Bangladesh*

Abstract

The correlation between the dielectric properties and the structural characteristics of Ta_2O_5 (Tantalum Oxide) doped $BaTiO_3$ (Barium Titanate) ceramics were investigated under different sintering conditions in this research. The raw materials of making Tantalum Oxide doped Barium Titanate were Ta_2O_5 and $BaTiO_3$ powders (particle size =100nm; purity better than 99%).Ta_2O_5 was doped at two different percentages viz. 0.5 and 1.0 mol%. Microstructure and fracture surface of sintered pellets were examined by a Scanning Electron Microscope (SEM). Dielectric properties were investigated by measuring the dielectric constant (k) as a function of temperature and frequency using an impedance analyzer. The results divulge that dielectric properties and microstructure of $BaTiO_3$ ceramics were significantly influenced by the addition of a small amount of Ta_2O_5. Percent theoretical density above 90% was achieved in this research for 0.5 and 1.0 mol% Ta_2O_5 doped $BaTiO_3$. It was observed that the grain size decreased markedly above a doping concentration of 0·5 mol% Ta_2O_5. Although fine grain size down to 200-300nm was attained, grain sizes in the range of 1-1.8µm showed the most alluring properties. The fine-grain quality and high density of the Ta_2O_5 doped $BaTiO_3$ ceramic resulted in tenfold increase of dielectric constant. Stable value of dielectric constant, as high as 13000-14000 in the temperature range of 55 to 80°C was found for 1.0 mol% Ta_2O_5 doped $BaTiO_3$ with corresponding shift of Curie point to ~80°C. Experimental results reveal that incorporation of a proper content of Ta_2O_5 in $BaTiO_3$ could control the grain growth, shift the Curie temperature and hence significantly improve the dielectric property of the $BaTiO_3$ ceramics..

Keywords: Barium Titanate, Tantalum Oxide Doping, Microstructure, Frequency, Dielectric Constant

1. Introduction

Barium Titanate ($BaTiO_3$) is the first ferroelectric ceramics and a good candidate for a variety of applications due to its excellent dielectric, ferroelectric and piezoelectric properties. It is extensively used in high dielectric constant capacitors, MLCC and energy storage devices. $BaTiO_3$ having the perovskite structure with tetragonal symmetry at room temperature, possesses a relatively high dielectric constant (~1500-2000).

Despite the advantage offered by the $BaTiO_3$ ceramic regarding small sized capacitors, their use is limited by a number of operating variables. The electric field strength and the operating temperatures are strong determinants of dielectric constants. Moreover, grain size has a significant effect on dielectric property of $BaTiO_3$ ceramics. Fine-grained $BaTiO_3$ with an average grain size of ~1µm exhibits dielectric constant of 3000-4000 at room temperature [1-5] and values as high as 6000 have also been reported [6]. According to Kinoshinto and Yamaji, as the grain size decreases the dielectric constant of

* Rubayyat Mahbub. Tel.:+880 1717 46 47 56.
E-mail address: turjo62000@hotmail.com

the material increases and a general broadening of the transition peak results [7]. Furthermore Martirena and Burfoot suggested that the room temperature permittivity of $BaTiO_3$ should significantly increase when the peak of the transition region is suppressed [8].

The dependence on temperature along with other properties can be appreciably modified by forming solid solutions or doping the base perovskite with a range of compositions. Recent research involves development of $BaTiO_3$ based ceramics with high dielectric properties using various doping elements of different concentrations [9-17]. The effect of Ta_2O_5 (Tantalum Oxide) doping in $BaTiO_3$ ceramic materials has shown promising dielectric properties. In addition, Yoeng Jung Kim et al. [18] have suggested that Ta^{5+} inhibits grain growth and when added in small amounts promote densification.

The objective of this investigation was to examine the effects of small additions of Ta_2O_5 on the microstructure and dielectric properties of pure $BaTiO_3$, and furthermore to establish a proper structure-property relationship.

2. Experimental

The starting materials of making Tantalum doped Barium Titanate were $BaTiO_3$ (size =100nm) and Ta_2O_5 powders [Manufacturer: INFRAMAT (USA); Purity better than 99%].Ta_2O_5 was doped at two different percentage viz. 0.5 and 1.0 mol%. The powders were milled in the pot mill containing Yttria stabilized zirconia balls for 16-20 hours, while a sufficient amount of acetone was added as the milling media. PVA was added as a binder following the drying process and the mixture was stirred for 30-40 minute to ensure a homogenous binder distribution. The mix was then dried and pressed into disc shaped samples under 2 tons of load. Next, the samples were soaked for binder removal and different sintering cycles were performed. Microstructure and fracture surface of sintered pellets were examined by a Scanning Electron Microscope (SEM). Temperature dependence of the dielectric constant was measured at various frequencies at a heating rate of 4^{o}C/min using an impedance analyzer (WAYNE KERR 6500B series).

3. Results and Discussion

Numerical data of percent theoretical density (%TD) and grain size of 0.5 and 1.0 mol% Ta_2O_5 doped $BaTiO_3$ sintered at 1250, 1275 and 1300°C for zero minute with a sintering rate of 5°C/min are tabulated in [Table. 1].

The sintering cycle with a sintering rate of 5°C/min yielded better densification for both doping mol% with optimum density and grain size for 0.5 mol% Ta_2O_5 doped $BaTiO_3$ sintered at 1300°C for zero minutes. The average grain size of the samples sintered at 1250°C were in the range 0.18-0.25µm for both 0.5 and 1.0 doping mol%, which as a result of being too fine, had an adverse effect on the dielectric properties. Grain size of samples sintered at 1275°C and 1300°C were relatively coarser with satisfactory densification. The microstructures of these samples sintered at 1275°C and 1300°C for zero minutes are shown in Fig. 1

[Table 1.] Percent theoretical density (%TD) and grain size of sintered Ta_2O_5 doped $BaTiO_3$ samples

Serial No.	Sintering Rate (°C/min)	Maximum Sintering Temp. (°C)	Holding Time (min)	Cooling Rate (°C/min)	Doping mol%	% TD	Grain Size (µm)
1	5	1250	0	3	0.5	95.45	.18-.3
					1.0	91.25	.18-.3
2	5	1275	0	3	0.5	97	.358
					1.0	92.65	.255
3	5	1300	0	3	0.5	97.66	1.6
					1.0	96.44	.295

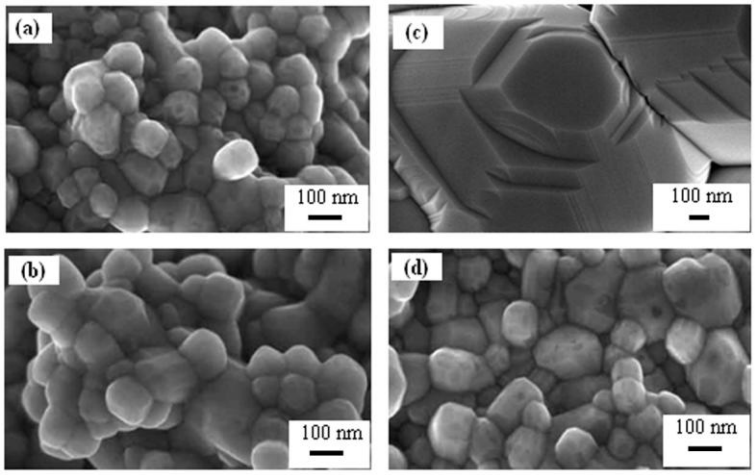

(a)Avg. Grain Size = 0.358 µm; % TD = 97 (b) Avg. Grain Size = 0.255 µm; % TD = 92.65
(c)Avg. Grain Size = 1.6 µm; % TD = 97.66 (d) Avg. Grain Size = 0.295 µm; % TD = 96.44

[Fig. 1.]SEM micrograph of (a) 0.5 mol% and (b)1.0 mol% Ta_2O_5 doped $BaTiO_3$ sintered at 1275°C for 0 minute and (c) 0.5 mol% and (d)1.0 mol% Ta_2O_5 doped $BaTiO_3$ sintered at 1300°C for 0 minute

Less porous and dense micrographs were obtained for all the samples sintered at 5°C/min. The time provided for sintering was sufficient as slower sintering rate of 5°C/min provided longer sintering time. Though optimum density and grain size were attained for 0.5 mol% Ta_2O_5 doped $BaTiO_3$ sintered at 1300°C for zero minutes, but for doping 1.0 mol% Ta_2O_5 the grain size reduced prominently (<0.5µm) for sintering rate of 5°C/min.

These results are commensurate with the findings of M.N. Rahman and R.Manalert [20] as they reported that for the penta-valance donor cations, the boundary mobility initially increases with cation concentration but then decreases markedly above a doping threshold of 0·3-0·5 mol%. This factor significantly controls the microstructure of Ta_2O_5 doped $BaTiO_3$.Since Ta^{5+} ion has a valence state (+5) different than that of Ba^{2+} or Ti^{4+} ions (+2 and +4 respectively), substitution with Ta^{5+} ions cause charge imbalance which leads to charge compensation requiring the production of electrons, electron holes, or vacancies. Donor cations of higher valence than the host cation leads to a dramatic change in the behavior of $BaTiO_3$. This phenomenon is sometimes referred to as the 'doping anomaly' or 'grain size anomaly' [18,19,20].

Below the doping threshold, a possible defect reaction for the incorporation of Ta^{5+}into $BaTiO_3$ can be written in the Kroger-Vink notation as equation (1). [20]

$$4BaO + 2Ta_2O_5 \rightarrow 4Ba_{Ba}^{X} + 4Ta_{Ti} + 12O_o^{X} + O_2 + 4e- \quad (1)$$

Above the doping threshold, assuming that ionic compensation occurs by the formation of Ti vacancies, a possible defect reaction is: [20]

$$4BaO + 2Ta_2O_5 + BaTiO_3 \rightarrow 5Ba_{Ba}^{X} + 4Ta_{Ti} + 15O_o^{X} + TiO_2 + V_{Ti} \quad (2)$$

Above the threshold, the accumulation of Ti vacancies in the space charge may be associated with a depletion of oxygen vacancies. Because of their relatively large size, the diffusivity of oxygen ions across the grain boundary is expected to be slow. The low diffusivity of oxygen ions across the grain boundary provides a possible mechanism for the significant reduction in grain boundary mobility, which yields finer grain. Such grain growth inhibiting mechanism has also been evident in the study of $BaTiO_3$ doped simultaneously with calcium (Ca^{2+}) and tantalum (Ta^{5+}) ions [19, 20]. In this study, replacement of V_{Ti} with Ca^{2+} was found to negate the grain growth inhibiting effect of Ta^{5+}.

The effect of excess doping mol% of Ta_2O_5 above the threshold value on microstructure of $BaTiO_3$ can also be described by using another perspective other than through the defect structure. Excess doping mol% of penta-valence donor cations

above the threshold is found to restrict grain growth by pinning effect [18]. Our results are in accordance with this finding also.

In our research, above the threshold value of 0.5 mol% doping, the grain size reduced prominently (<0.5µm) for sintering rate of 5°C/min which can be attributed to the pinning effect of excessive Ta_2O_5 doping above the threshold value [18, 20]. A high concentration of Ta^{5+}ions at or near grain boundaries restricted grain growth during sintering and promoted the formation of $BaTiO_3$ with extremely fine grains. Such small grain size has an adverse effect on dielectric properties.

No or insignificant energy is needed for the dopant to concentrate at the grain boundaries. However, the energy needed to incorporate a dopant ion into an individual lattice site in complex oxides is related to distortions, i.e. difference in ionic radii, and the formation of compensating defects during the incorporation of aliovalent ions that have different valence states [18]. Thus, more energy was required in our research for diffusion of the dopants to move inwards from the grain boundary and reduce the extreme pinning effect. The required energy was provided by means of increasing the holding time to 240 minutes at the maximum sintering temperature of $1300^{O}C$ for both dopant concentrations. To control abnormal grain growth, sintering rate was increased to15°C/min and the cooling rate was also modified [Table. 2].The microstructures of 0.5 and 1.0 mol% Ta_2O_5 doped $BaTiO_3$ sintered under this condition is shown in [Fig. 2.].

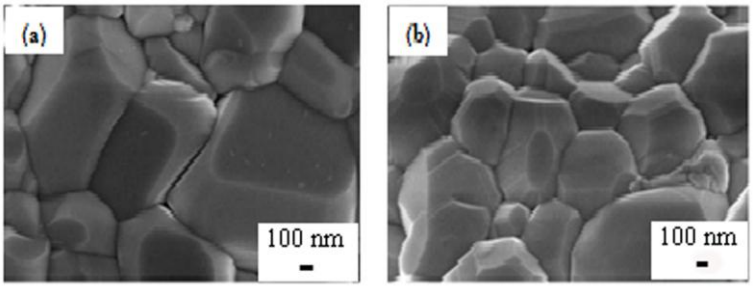

[Fig. 2.]SEM micrograph of a) 0.5 mol% & b) 1.0 mol% Ta_2O_5 doped $BaTiO_3$ sintered at 1300°C for 240min

[Table 2.] Percent theoretical density (%TD) and grain size obtained for the modified sintering cycle

Sintering Rate (°C/min)	Maximum Sintering Temp. (°C)	Holding Time (min)	Cooling Rate (°C/min)	Doping mol%	% TD	Grain Size (µm)
15	1300	240	10 °C/min up to 1000°C and then 5 °C/min up to end temperature	0.5	91	1.8
15	1300	240	10 °C/min up to 1000°C and then 5 °C/min up to end temperature	1.0	90	1.375

3.1 Dielectric Property Measurement

0.5 mol% Ta_2O_5 doped $BaTiO_3$ sintered at 1300°C for 0 min at sintering rate 5°C/min and 1 mol% Ta_2O_5 doped $BaTiO_3$ sintered at 1300°C for 240 min at sintering rate 15°C/min showed satisfactory dielectric constant along with desired densification and grain size [Table. 3.].

[Table 3.] % Theoretical density (%TD), grain size and dielectric constant of sample sintered at optimum sintering cycles

Serial No.	Sintering Rate (°C/min)	Maximum Sintering Temp. (°C)	Holding Time (min)	Cooling Rate (°C/min)	Doping mol%	% TD	Grain Size (µm)	Dielectric Constant (k) Value (room temp.)
1	5	1300	0	3	0.5	97.66	1.6	14600
2	5	1300	0	3	1.0	96.44	.358	1900-2000
3	15	1300	240	10 °C/min up to 1000°C and then 5 °C/min up to end temperature	0.5	90	1.8	14000
4	15	1300	240		1.0	91	1.375	17000

[Fig. 3] illustrates that sintering at 1300°C for 240 min at a sintering rate of 15°C/min resulted in an abrupt rise in dielectric constant for 1.0 mol% Ta_2O_5 doped $BaTiO_3$ which was due to attainment of favorable grain size and densification. However, a slight declivity in dielectric constant was observed for 0.5 mol% Ta_2O_5 doped $BaTiO_3$ when the holding time was increased to 240 min at 1300°C. Sintering at 1300°C for 240 min at sintering rate 15°C/min caused only a slight increase in grain size, from 1.6 to 1.8µm, together with marked attenuation of densification for 0.5 mol% Ta_2O_5 doped $BaTiO_3$ as reported in [Table. 3]. Hence, for 0.5 mol% Ta_2O_5 doped $BaTiO_3$ the maximum dielectric constant, together with approbative grain size and densification was obtained when sintered at 1300°C for 0 min at sintering rate 5°C/min.

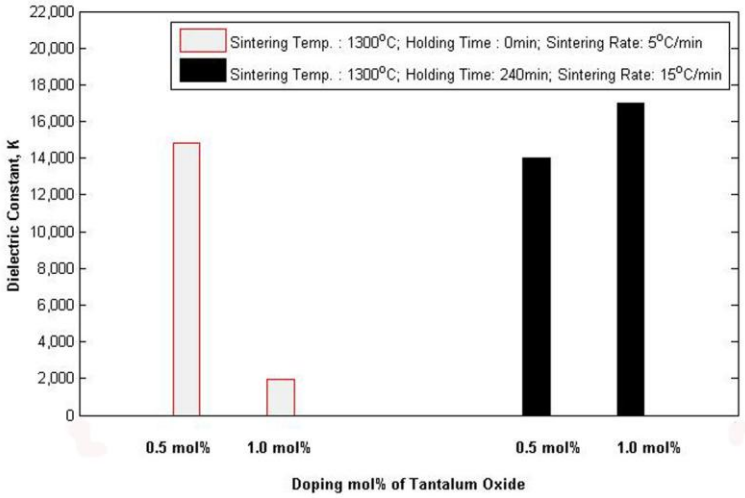

[Fig. 3.]Dielectric constant of samples sintered at optimum sintering cycles

The pinning effect or influence on defect structure of doping mol% was found to effect grain size. As grain size effect dielectric properties, so pinning effect or influence on defect structure of dopants has obvious effect on dielectric properties. Average grain size around 1µm normally provides a good condition for dielectric properties for doped $BaTiO_3$. In this research, grain sizes in the range of 1-1.4µm showed high values of dielectric constant, while further increase in grain size deteriorated its property. Variation of Dielectric Constant (k) with temperature for 0.5 and 1 mol% Ta_2O_5 doped $BaTiO_3$ that have a maximum dielectric constant is shown in [Fig. 4]. The best stable value of dielectric constant as a fucntion of temperature was obtained in the range 13000-14000 for 1.0 mol% Ta_2O_5 doped $BaTiO_3$ as shown in [Fig. 4(b).]. Curie point (Tc) normally occurs at 120°C for pure $BaTiO_3$. It is evident from [Fig. 4] that the curie point was shifted to about 110^OC for 0.5 mol% Ta_2O_5 doped $BaTiO_3$; and to about 80^OC for 1 mol% Ta_2O_5 doped $BaTiO_3$. Suppression of the peak at Curie temperature is also apparent from the figure. In consonant with the literature [21,22,23], a decrease in dielectric contstant with an increase of frequency for a particular temperature is also ostensible from the figure.

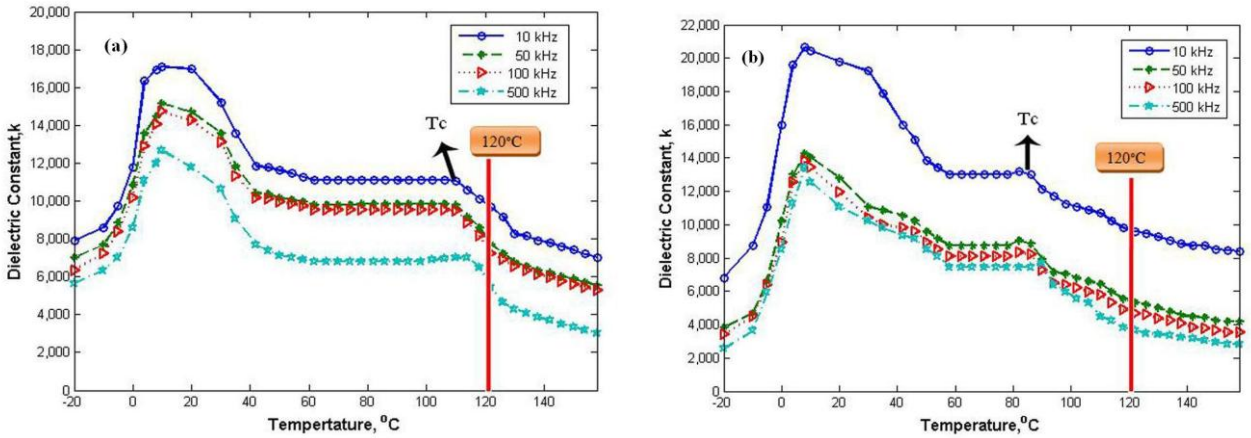

[Fig. 4.]Variation of k with temperature for (a) 0.5mol% Ta_2O_5 doped $BaTiO_3$ sintered at 1300°C for 0 min at sintering rate10°C/min(b) 1.0mol% Ta_2O_5 doped $BaTiO_3$ sintered at 1300°C for 240 min at sintering rate15°C/min

4. Conclusions

The results reveal that doped tantalum oxide acts as a strong peak suppressor and shifts the Curie point to a lower temperature. Alluring value of dielectric constant was obtained when average grain size of the Ta_2O_5 doped $BaTiO_3$ samples were in the range of 1-1.8µm and the best stable value as high as 13000-14000 in the temperature range of 55 to 80°C was obtained for 1.0 mol% Ta_2O_5 doped $BaTiO_3$ having an average grain size of 1.375µm, with corresponding shift of Curie point to ~80°C. Moreover it was observed that, for a particular temperature the value of dielectric constant decreases with an increase of the applied frequency.

Acknowledgements

The authors acknowledge to Mr. Tan Teck Siong, JEOL Asia Pte Ltd for his assistance in SEM analysis.

References

[1] HH. Kniepkamp and W. Heywang, 1954. Depolarization Effects in Polycrystalline, $BaTiO_3$, Z. Angrew. Physics.6, p. 385-90.
[2] A.S. Shaikh, R.W.Vest, and G. M.Vest, 1986. Dielectric Properties of Ultra Fine Grained $BaTiO_3$, In: IEEE International Svmosium on Applied Ferroelectrics. 6th, p. 126-29.
[3] G. H. Jonkkr and W. Noorland, 1962. Grain Size of Sintered Barium Titanate, In: Science of Ceramics 1, Edited by G. H. Stewart, Academic Press, London, p. 255-64.
[4] N. C. Sharma and E. R. McCartney, 1974. The Dielectric Properties of Pure Barium Titanate as a Function of Grain Size, Journal of Australasian Ceramic Society, 10 [I61], p. 16-20.
[5] G. Arlt, D. Hennings, and G. de With, 1985. Dielectric Properties of Fine-Grained Barium Titanate Ceramics, Journal of Appied. Physics, 58 [41], p.1619-25.
[6] A. A. Anan'eva, M. A. Ugryumova and B.V. Strizhkov,1960, Some Anomalous Properties of Chemically Pure Barium Titanate Ceramic. Bulletin of Academy of Science (Engl. Transl.), 24, p. 1395-97.
[7] K. Kinoshinta and A. Yamaji,1976. Grain-Size Effects on Dielectric Properties in Barium Titanate, Journal of Applied Physics, 47 [I], p. 371-74.
[8] H. T. Martirena and J. C. Burfoot, 1974. Grain-Size Effects on Properties of Some Ferroelectrics Ceramics, Journal of Physics Society, C,7, p.3182-92.
[9] Liang X., MengZ.and Wu W., 2004. Effect of acceptor and donor dopants on the dielectric and tunable properties of barium strontium titanate, Journal of American Ceramic Society, 86(12), p. 2218-2222.
[10] Babilo P. and Haile S.M., 2005. Enhanced sintering of Yuttrium-doped barium zirconate by addition of ZnO, Journal of American Ceramic Society, 88(9), p.2362-2368.

[11] Hamady Yassen, Sioma Baltianski and Yoed Tsur., 2006. Effect of incorporating method of niobium on the properties of doped Barium Titanate Ceramics, Journal of American Ceramic Society, 89[5], p.1584-1589.

[12] V.V.Mitic and I. Mitrovic, 2001. The influence of Nb_2O_5 on $BatiO_3$ ceramics dielectric properties, Journal of American Ceramic Society,21.

[13] K. H. YOON, J. W. KIM, K. H. JO, 1989. Dielectric properties of barium titanate with Sb_20_3 and ZnO, Journal of Materials Science Letters, 8, p.153-156.

[14] Yogeswar Kumar et. al., December 2009. Effect of Ni doping in structural and dielectric properties of $BaTiO_3$, Indian Journal of Engineering and Materials Science, Vol. 16, p.390-394.

[15] Jirapa Tangsritrakul, Rattikorn Yimnirun, 2010.Effects of Manganese Addition on Phase Formation and Microstructure of Barium Titanate Ceramics, Chiang Mai Journal of Science, 37(1), p.165-169.

[16] Timothy R. Armstrong, Laurie E.Morgens, Alena K. Maurice and Relva C. Buchanan*, 1989. Effects of Zirconia on Microstructure and Dielectric Properties of Barium TitanateCeramics, Journal of American Ceramic Society, [4], p. 605-11.

[17] Sabina Yasmin, Shamima Choudhury, M.A. Hakim, A.H. Bhuiyan and M.J.Rahman, 2011. Structural and Dielectric Properties of pure and cerium doped barium titanate, Journal of Ceram.Processing Research, Vol. 12, No. 4, p. 387-391.

[18] Yoeng Jung Kim, June Won Hyun, HeeSoo Kim. Joo Ho Lee, Mi Young Yun. S.J. Noh and Yong Hyun Ahn, 2009. Microstructural characterization and dielectric properties of barium titanate solid solution with donor dopants, Bulletin of Korean Chemical Society,Vol. 30, No. 6, p.1268-1273.

[19] Helen M.Chan, Martin P. Harmer and Donald M. Smyth,1986. Compensating Defects in Highly Donor-Doped $BaTiO_3$, Journal of American Cermic Society, 69[6], p.507-10.

[20] M.N.Rahman and R.Manalert, 1988. Grain Boundry Mobility of $BaTiO_3$ Doped with Aliovalent Cations, Journal of European Ceramic Society, 18, p. 1063-1071.

[21] C. Barry Carter, M. Grant Norton., "Ceramic materials science and engineering", published by springer.

[22] Kingery, Bowen, Uhlman: Introduction to Ceramics, John Willey & Sons, second edition, Singapore, 1976

[23] Richerson: Modern Ceramic Engineering, Marcel Dekker, 1992